Decays of the Heavy Lepton, Tau (1785)

Craig A. Blocker

Abstract

The structure of the weak hadronic current coupled to the tau is investigated via some of the hadronic decays of the tau. The vector current coulping is determined by measuring the $\tau \to \rho\nu_\tau$ branching ratio. The axial-vector coupling is determined by measuring the $\tau \to \pi\nu_\tau$ branching ratio. The Cabibbo structure of the hadronic current is established by observing the decay $\tau \to K^*(890)\nu_\tau$ and measuring its branching ratio. The branching ratios for the decays $\tau \to e\bar{\nu}_e\nu_\tau$ and $\tau \to \mu\bar{\nu}_\mu\nu_\tau$ are measured as a normalization for the hadronic decays and as a check on the validity of the measurements. The leptonic branching ratios agree well with previous experiments.

From a kinematic fit to the pion energy spectrum in the decay $\tau \to \pi\nu_\tau$, an upper limit (95% confidence level) of 245 MeV is placed on the tau neutrino mass. From a simultaneous fit of the center of mass energy dependence of the tau production cross section and the pion energy spectrum in the decay $\tau \to \pi\nu_\tau$, the tau mass is determined to be $1.787 \pm .010$ GeV/c .

All properties of the tau measured here are consistent with it being a sequential lepton coupled to the ordinary weak hadronic current.

DEDICATION

I dedicate this dissertation to the memory of Mom.

ACKNOWLEDGEMENTS

I wish to thank the talented members of the SLAC-LBL Mark II collaboration, without whose effort an experiment of the Mark II's complexity and quality would not have been possible. I must single out Dr. J. Dorfan who provided the inspiration for this work along with continued interest and valuable discussions.

On the personal side, I would like to thank Dad for his support and understanding and to thank Claudia for enhancing the human side of my graduate education.

TABLE OF CONTENTS

Chapter I

INTRODUCTION

The study of e+e- annihilations at center of mass energies from 3-7.5 GeV has been an extremely rich and interesting field during the past five years. Two discoveries have been particularly spectacular- the charm quark with its associated complex spectroscopy and a new lepton, the tau. This thesis explores the production and decay of the tau at the SLAC e+e- storage ring facility SPEAR in order to understand the tau's properties and interactions.

Before the discovery of the tau, the only known leptons were the electron, the electron neutrino, the muon, and the muon neutrino. These leptons couple to other particles via interactions which are thought to be well understood, namely, the weak and electromagnetic interactions. It is vital to study to the couplings of the tau to understand whether it simply mimics the other leptons or is indicative of new phenomena or interactions. Previous studies of the tau have primarily utilized its leptonic decays, and a thorough understanding of its coupling to hadrons is lacking.

In this dissertation, the structure of the hadronic current coupled to the tau is studied in detail via three

of its hadronic decays, namely[1], $\tau \to \rho\nu$, $\tau \to \pi\nu$, and $\tau \to K^*(890)\nu$. If the possibility of arbitrary scalar (S), pseudo-scalar (P), vector (V), axial-vector (A), and tensor (T) couplings is allowed, it is not possible here to draw definative conclusions about the hadronic current. However, there is strong theoretical prejudice for a V,A structure, and that will be assumed. Then the $\tau \to \rho\nu$ decay occurs via the vector current, and the $\tau \to \pi\nu$ decay occurs via the axial vector current, allowing separation and study of these two couplings. The $\tau \to K^*\nu$ decay also occurs via the vector current and, in conjunction with the $\tau \to \pi\nu$ decay, gives the Cabibbo structure of the hadronic current. The leptonic decays of the tau are also measured here to provide a normalization for hadronic decays and as a check on the validity of the measurements.

A major advantage e+e- experiments have over hadronic experiments is the simplicity of the initial state, that is, two leptons which annihilate into one virtual photon via the well understood electromagnetic interaction (Fig. 1), allowing isolation and study of the production and subsequent decay of particles (both leptons and hadrons) at the second vertex. The price that is paid for the simplicity of the initial state is the low event rates typical of e+e- storage rings. For the tau cross section and a typical average luminosity[2] at SPEAR, about 200-500 tau pairs were produced per day of running.

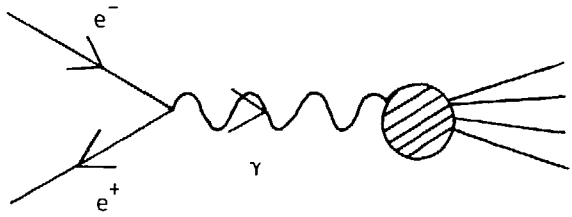

Fig. 1. e^+e^- annihilation via a single virtual photon.

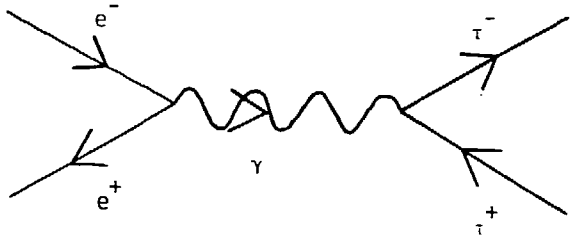

Fig. 2. Feynman diagram for $e^+e^- \rightarrow \tau^+\tau^-$.

1.1 HISTORY AND PROPERTIES

The initial evidence for a new lepton was the observation[3] by the SLAC-LBL collaboration at the e+e- colliding beam facility SPEAR of anomalous lepton events of the form $e^+e^- \rightarrow e^{\pm} + \mu^{\mp}$ + "missing energy". Subsequently, this anomalous lepton production was confirmed by several experiments[4 5 6 7], and the properties of these events firmly established that the anomalous leptons were from the production and decay of a new lepton, now designated tau.

Once the existence of the tau was established, it became important to measure its properties in order to understand its place in the particle world. Some of these properties have already been well measured. The mass has been determined[8 9 10] from the threshold behavior of the tau production cross section. The measurement with the smallest error is DELCO's vaule of $1.782^{+.002}_{-.007}$ GeV/c^2. From the high energy rise of this cross section, Tsai[11] argues that only a spin 1/2, pointlike tau is consistent with the data. All experiments hav favored a V-A coupling to the weak current for the tau, but the DELCO measurement[12] of the Michel parameter using the electron spectrum from tau decays provides the strongest evidence. It favors V-A, is inconsistent with V+A, and strongly disfavors pure V or A. The neutrino associated with the tau appears to be different from the electron or muon neutrino or antineutrinos[4 8 13 14 15] and to be massless (the upper limit[12] is .25 GeV/c^2, 95% confidence level).

The picture that emerges is that the tau is a sequential lepton, that is, a spin 1/2, pointlike particle with its own lepton number, its own neutrino, and a V-A coupling of the same strength as other leptons to the conventional weak current. There are other possibilities having a massive neutrino and electron-muon-tau mixing, but electron-muon universality place severe limitations on these models.[16] Throughout this thesis it was assumed that the tau is a sequential lepton with the DELCO mass of 1.782 GeV/c^2 and a massless neutrino.

1.2 THEORY

The existence of the muon has long been a puzzle in elementary particle physics in that it is not required by any theory. The current gauge theories of weak and electromagnetic interactions do require that the sum over the quark and lepton charges weighted by group theory phases be zero so that Adler triangle anomalies[17] cancel and the theory be renormalizable. The up and down quarks along with the electron form a satisfactory and complete theory. The addition of the strange and charm quarks and the muon again forms a collection of particles that satisfy the Adler condition. The discovery of the tau upset this balance which has been partially rectified by the discovery of the upsilon, which is most likely a charge 1/3 quark-antiquark state. However, there is no evidence yet in e+e-

annihilations up to 31 GeV for the charge 2/3 quark needed in the standard Weinberg-Salam model to restore the balance.

1.2.1 Production

Taus are produced as pairs via the Feynman diagram shown in Fig. 2 with a cross section of

$$\frac{d\sigma}{d\Omega} = \frac{\alpha^2}{4s}\beta(2-\beta^2+\beta^2\cos^2\theta)$$

$$\sigma_{\tau\tau} = \frac{2\pi\alpha^2\beta}{3s}(3-\beta^2)$$

where α is the fine structure constant ($\sim 1/137$), s is the square of the center of mass energy, and β is the velocity of the tau in units of the speed of light.

1.2.2 Decays

One property of the tau that distinguishes it from the other known leptons is that it is sufficiently massive to decay into hadrons, allowing tau decays to be used to test theories of hadronic weak interactions. Assuming the tau is a sequential lepton, many of the decay widths can be calculated[18 19 20] either exactly or to a good approximation.

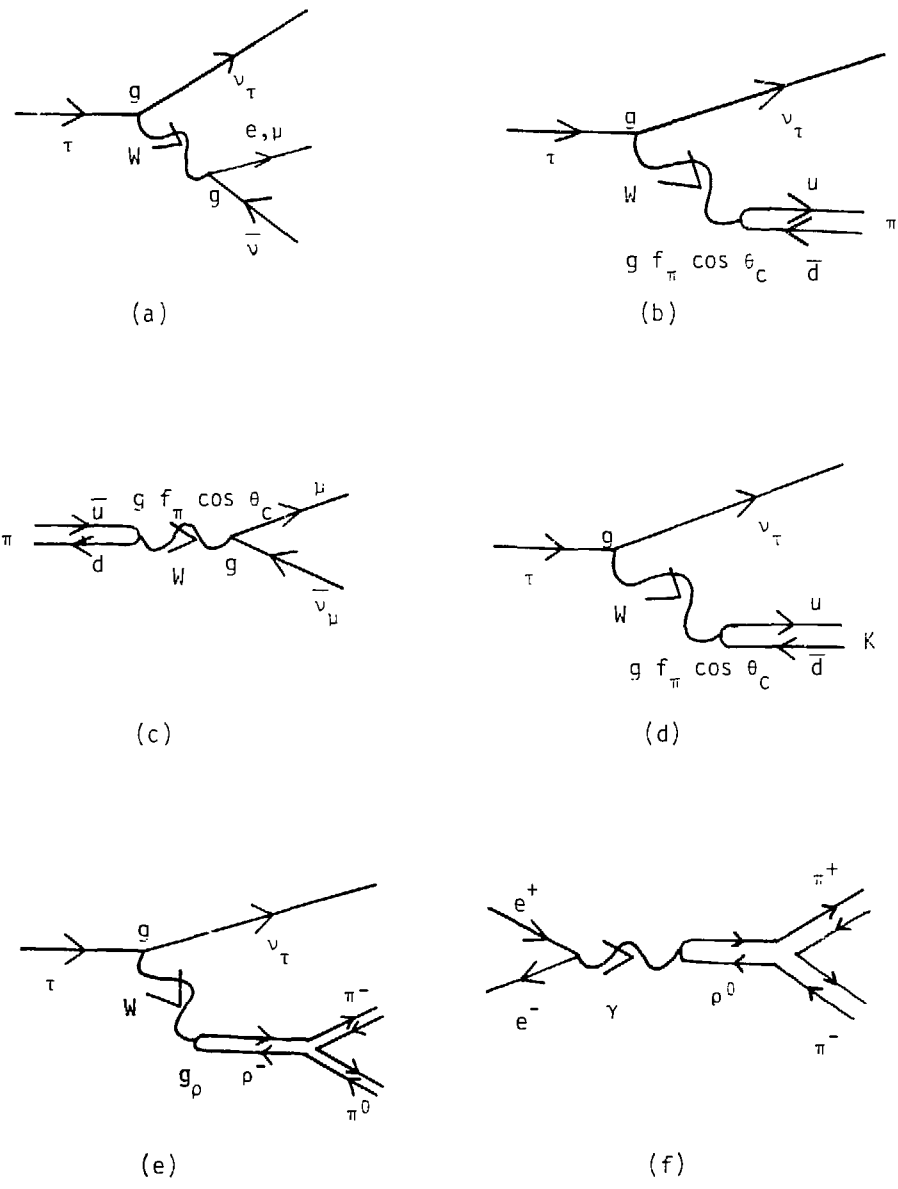

Fig. 3. Feynman diagrams for (a) $\tau_{\pm} \to \ell\nu\nu$, (b) $\tau \to \pi\nu$, (c) $\pi \to \mu\nu$, (d) $\tau \to K\nu$, (e) $\tau \to \rho\nu \to \pi^-\pi^0$, and (f) $e^+e^- \to \rho^0 \to \pi^+\pi^-$.

1 2.2.1 Leptonic decays

The leptonic decay widths are calculated from the Feynman diagram in Fig. 3a. A straight forward calculation[19] gives

$$\Gamma(\tau \to \ell \nu \nu) = \frac{G^2 M_\tau^5}{3 \times 2^6 \pi^3} [1-8y+8y^3-y^4-12y^2 \ln(y)]$$

where ℓ is either an electron or muon, G is the Fermi weak coupling constant known from mu decay, and y is defined as M_ℓ^2/M_τ^2. This calculation is exact to lowest order and depends only on known parameters. The factor in brackets is 1.000 for electrons and .973 for muons for a tau mass of 1.782 GeV/c^2.

1.2.2.2 Pion and kaon decay

The decay width for $\tau \to \pi\nu$ is calculated from Fig. 3b. Again, a straight forward calculation gives

$$\Gamma(\tau \to \pi\nu) = \frac{G^2 f_\pi^2 \cos^2\theta_c}{16\pi} M_\tau^3 (1-\frac{M_\pi^2}{M_\tau^2})^2$$

where θ_c is the Cabibbo angle. f_π is a constant in the pion form factor obtained from the decay rate for $\pi \to \mu\nu$, which proceeds through a similar diagram, as shown in Fig. 3c. Its value is .137 times the mass of the proton.

The diagram (Fig. 3d) for the decay $\tau \to K\nu$ is identical except that the pion is replaced by a kaon and cos θ_c

is replaced by sin θ_c . This immediately gives

$$\Gamma(\tau \to K\nu) = \frac{G^2 f_\pi^2 \sin^2\theta_c M_\tau^3}{16\pi}(1-\frac{M_K^2}{M_\tau^2})^2$$

The calculation of these widths is again exact to lowest order and depends only on known parameters.

1.2.2.3 Rho and other even pion decays

The decay $\tau \to \pi\pi\nu$ also proceeds through a very similar diagram (Fig. 3e), but now the W-rho coupling is not directly known since the rho does not decay weakly. However, since the rho is a vector particle, only the vector portion of the weak current contributes, and the W-rho coupling can be related to the gamma-rho coupling via the conserved vector current hypothesis (CVC). The gamma-rho coupling is obtained from measurements of $e^+e^- \to \rho^0 \to \pi^+\pi^-$ which proceeds as in Fig. 3f. There could also be a small non-resonant contribution to $\tau \to \pi^-\pi^0\nu$ and $e^+e^- \to \pi^+\pi^-$ where the rho in Figs. 3e and 3f is absent. Gilman and Miller[19] calculate for a tau of mass 1.8 GeV/c^2 that $\Gamma_{\rho\nu}/\Gamma_{e\nu\nu}$ = 1.2 for pion pairs that have an invariant mass less than 1.25 GeV/c^2. The rho resonance is expected to dominate the two pion decays of the tau. Using the same technique of assuming CVC and using e+e- data the width for $\tau \to 4\pi\nu$ is .57 $\Gamma(\tau \to e\nu\nu)$. Gilman and Miller[20] calculate that for a tau mass of 1.8 GeV/c^2

$$\Gamma(\tau^- \to \pi^-\pi^-\pi^+\pi^0\nu) = .46\ \Gamma(\tau \to e\nu\nu)$$

$$\Gamma(\tau^- \to \pi^- 3\pi^0\nu) = .11\ \Gamma(\tau \to e\nu\nu).$$

The accuracy of these calculations depends on the measurements of $e^+e^- \to 2n^-$ which are good to 10-20% for the two pion case and on the assumption of CVC. Thus, measuring these decay widths provides a test of the applicability of the CVC hypothesis to tau decays.

1.2.2.4 Al decay

Assuming that the Al exists and dominates the $\tau \to 3\pi$ decays, Tsai[19] has calculated from Weinberg sum rules that

$$\Gamma(\tau \to A_1 \nu) = \frac{G^2 M_\tau^3 \cos^2\theta_c}{256\pi^3} c_{M_{A1}} \left(1-\frac{M_{A1}^2}{M_\tau^2}\right)^2 \left(1+\frac{2M_{A1}^2}{M_\tau^2}\right)$$

This depends only on known parameters but is more uncertain than other widths due to some of the assumptions in the derivation. In particular, the existence of the Al is uncertain. Measurement of the rate and distributions of the $\tau \to 3\pi$ decay could settle the question of the Al's existence.

1.2.2.5 K*(892) and Q(1313) decays

Using Das-Mathur-Okubo sum rules, Tsai[19] has calculated for the strange counterparts to the rho and Al that

$$\Gamma(\tau \to K^* \nu) = \Gamma(\tau \to \rho \nu) \tan^2\theta_c \left(1-\frac{M_{K^*}^2}{M_\tau^2}\right)^2 \left(1+\frac{2M_{K^*}^2}{M_\tau^2}\right) / \left(1-\frac{M_\rho^2}{M_\tau^2}\right)^2 \left(1+\frac{2M_\rho^2}{M_\tau^2}\right)$$

$$\Gamma(\tau \to Q \nu) = \Gamma(\tau \to \rho \nu) \tan^2\theta_c \frac{M_{K^*}^2}{M_Q^2} \left(1-\frac{M_Q^2}{M_\tau^2}\right)^2 \left(1+\frac{2M_Q^2}{M_\tau^2}\right) / \left(1-\frac{M_\rho^2}{M_\tau^2}\right)^2 \left(1+\frac{2M_\rho^2}{M_\tau^2}\right)$$

These are Cabibbo suppressed decays and accordingly have small widths.

1.2.2.6 Summary

Table 1 summarizes the theoretical predictions for the decay widths, the corresponding branching ratios, and the experimental values. The world average for the leptonic widths agrees well with the theoretical expectation. The early measurement[24] of the pion decay mode indicated that it was smaller than expected, but later measurements[11,16,17,18] were closer to expectations. The other modes agree roughly but have large errors, or there is essentially no measurement. Experimentally, what is measured is the branching ratio ($= \Gamma_i / \Gamma_{tot}$). Even in cases where the partial width can be calculated exactly, the theoretical calculation of the branching ratio is uncertain to the extent that the total width is uncertain. Since some of the multi-pion decays cannot be calculated exactly, the total width has some theoretical uncertainty. To make a more meaningful comparison with theory, all results in this thesis are given as the quotient of the branching ratio and the measured electronic branching ratio ($= B_i / B_{e\nu\nu}$), which is theoretically uncertain only to the extent that the partial width is uncertain.

It is interesting to compare these detailed calculations to the prediction of the lowest order quark model.

Assuming that the tau decays by emitting a W that materializes into a light quark pair ($u\bar{d}$) or a lepton pair ($e\nu$ or $\mu\nu$), the width to hadrons should be three times (because of three colors) that to an electron or muon, giving branching ratios $B_{e\nu} = B_{\mu\nu} = 1/3\ B_{hadrons} = .2$, which approximately agree with those in Table 1.

Decay Mode	Theory[22]			Experimental		
	Γ (10^{-13} sec^{-1})	B (%)	B/B_e	B (%)	B/B_e	Reference
$e\bar{\nu}\nu$	64.6	17.8	1.	16.5±1.5 17.5±1.2	1. 1.	23 24,41
$\mu\bar{\nu}\nu$	63.	17.3	.97	18.6±1.9 17.1±1.2	1.13±.16 ----	23 23,41
1 hadron	144.3	39.7	2.23	34.3±4.2 35.0±4.0	2.06 2.00	23 23,41
$\geq$3 hadrons	91.6	25.2	1.42	30.6±3.0 30.4±2.9	1.85 1.74	23 23,41
$\pi\nu$	36.	9.9	.56	2.0±2.5 9.3±3.9 9.0±3.5 8.0±3.5 8.0±1.9 8.2±2.5	.11±.14 .53±.23 .51±.17 .46±.18 .46±.06 .47±.11	24 23 41 37 24* 38*
$\rho\nu$	77.5	21.3	1.20	24±9 18.5±1.5	1.37±.51 1.11±.22	24,41 39*
$A_1\nu$ $\rightarrow\pi^-\pi^+\pi^-\nu$	33.7 16.9	9.3 4.6	.52 .26	5±2.1 7±5	.29±.09 .40±.29	8 43
$4\pi\nu$	36.8	10.1	.57	11±7	.63±.4	43
$\geq 5\pi\nu$	44.2	12.2	.68			
$K\nu$	2.6	.72	.04	<1.6	<.09	8
$K^*\nu$	5.1	1.4	.08			
Total	363.5	100.				

Table 1. Theoretical and experimental branching ratios for decays of the tau. *Mark II data used here.

Chapter II

THE MARK II DETECTOR

2.1 MARK II

The Mark II detector was designed as a general purpose detector for detecting both charged and neutral particles from electron-positron annihilations over the maximum solid angle possible. High detection efficiency, good resolution, and good particle identification were important considerations. The Mark II had a basically cylindrical geometry with the beam direction forming the symmetry axis. The coordinate system referred to in this thesis is such that the z axis is in the direction of the positron beam, the y axis is vertical, and the x axis completes the right-handed coordinate system. The origin is at the center of the detector where the electron and positron beams collide.

Figs. 4a and 4b show cross-sectional and isometric views of the Mark II detector. As a particle left the e+e- interaction region, it first traversed a .15 mm thick stainless steel beam pipe and then two layers of .64 cm thick cylindrical scintillators (pipe counters) which were used in the trigger. Next came 16 layers of cylindrical drift chambers (described in detail in Ref. 30) for charged particle tracking. The rms momentum resolution was

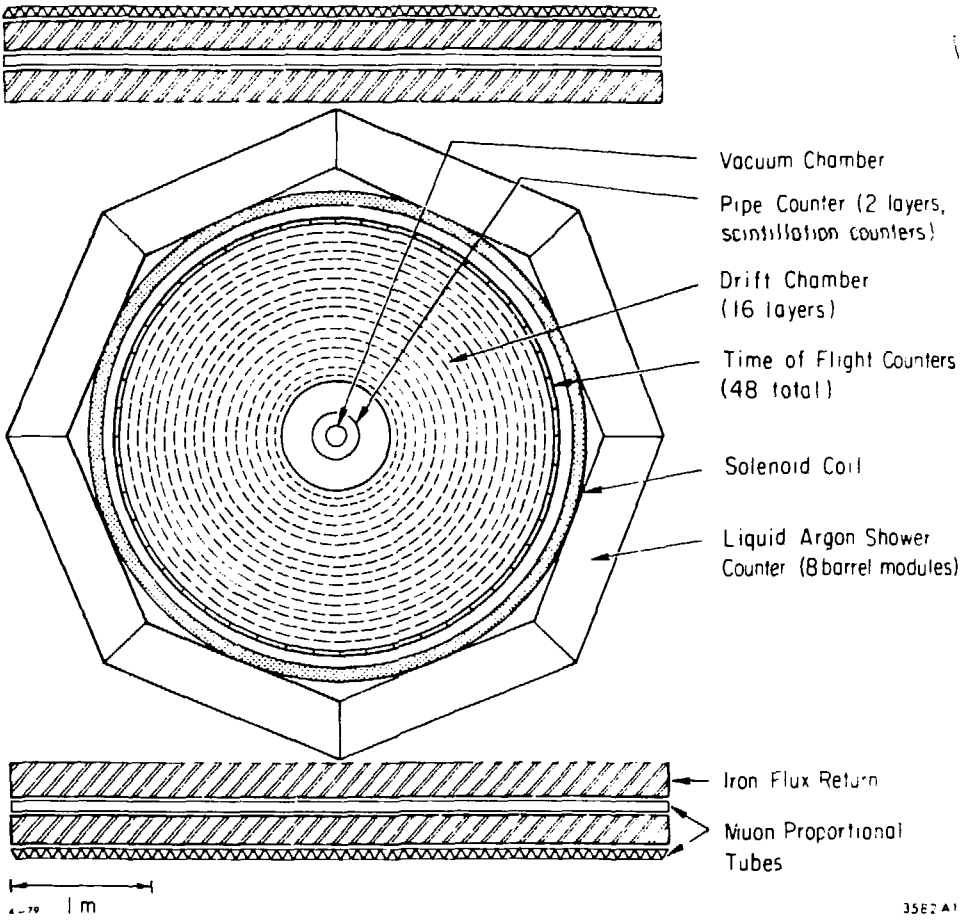

Fig. 4. (a) Cross sectional view of the Mark II detector.

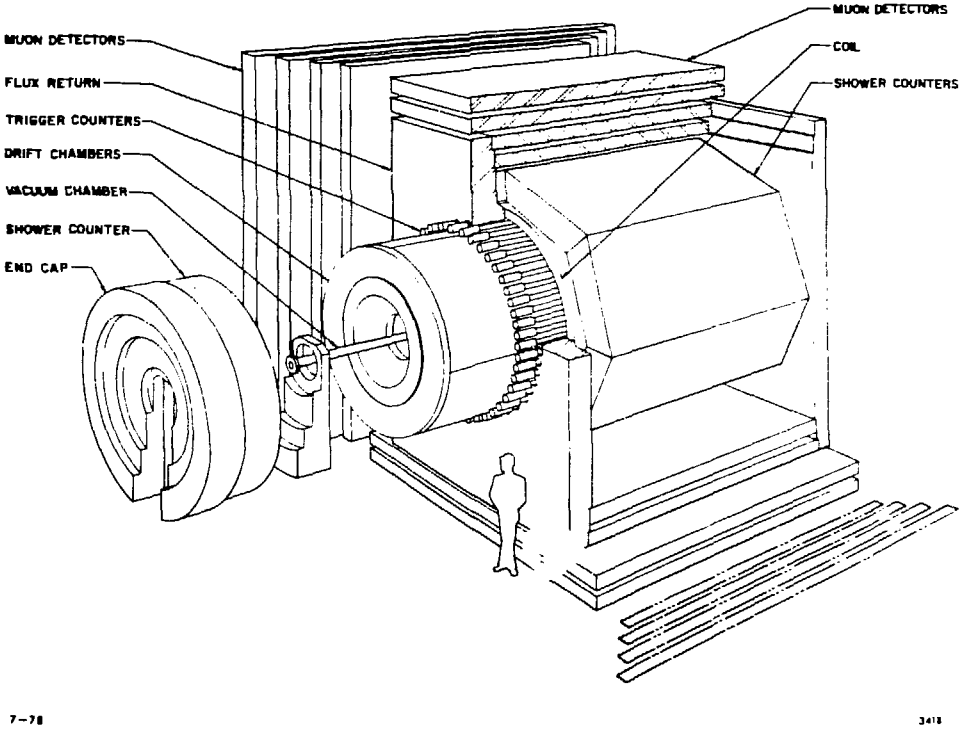

Fig. 4. (b) Expanded isometric view of the Mark II detector.

$\delta p/p = \sqrt{(.0145)^2 + (.010p)^2}$ (p in GeV/c) for single track fits. The factor of .0145 is from multiple scattering and the p dependent term reflects the 200 micron position resolution. Constraining the tracks to pass through the known beam position reduced the latter term to $(.005p)^2$.

Outside the drift chambers were 48 time-of-flight (TOF) scintillation counters which were 2.54 cm thick and viewed at both ends by photomultiplier tubes. The rms TOF resolution for electron-positron elastic scatters (Bhabha events) was 270 psec. and for hadrons was typically 300 psec measured from low momentum pions that were well separated in TOF from other particles. This gave a one standard deviation separation of pi's and K's at a momentum of 1.35 GeV/c. The TOF counters covered 75% of the full solid angle.

Outside the TOF system was the solenoidal magnet coil which provided a nearly uniform field of 4.1 kilogauss parallel to the e+e- beam direction. Next came the lead-liquid argon shower counters which provided photon detection and electron identification for 70% of the solid angle. The lead-liquid argon system is described in detail in Appendix B and the relevant characteristics are summarized here. The energy resolution was measured to be $11.5\%/\sqrt{E}$ (E in GeV) for electrons and high energy photons. For lower energy photons (a few hundred MeV), the energy resolution was a little higher ($12\text{-}13\%/\sqrt{E}$) due to uncertainties in the

corrections for loss of energy in the 1.4 radiation length thick magnet coil. The photon detection efficiency (Fig. 5) was calculated using the EGS[31] shower Monte Carlo to deposit energy according to the shower counter geometry and was checked using data from $\psi \to \pi^+\pi^-\pi^0$ and $\psi \to 2\pi^+2\pi^-\pi^0$ events.

Finally, there were layers of 23 cm thick steel, each followed by a plane of proportional counters, for muon identification above a momentum of approximately .65 GeV/c, the range threshold for muons. The initial configuration consisted of two layers on the top and bottom covering 24% of the solid angle. Later, one layer was added to the top and two layers to each side, extending the coverage to 54% of 4π sr.

At small angles to the beams were additional endcap shower counters. At one end was a liquid argon calorimeter, and at the other end were two layers of proportional chambers each proceeded by .5 cm of lead. Each endcap covered 10% of 4π sr.

The luminosity[1] was monitored with very small angle (~20 mrad) shower counters detecting Bhabha events. The final time integrated luminosities were determined from large angle Bhabha scatters. There was a 6% error assigned to the integrated luminosities due to uncertainties in event selection and in radiative corrections to the Bhabha scattering cross section.

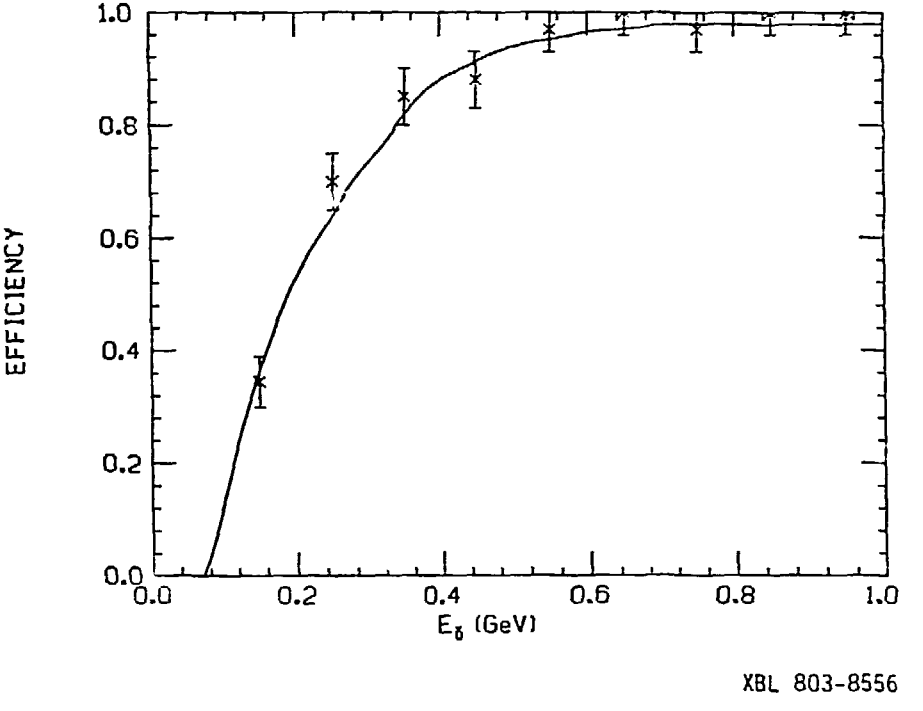

Fig. 5. Photon detection efficiency excluding geometry. Data points were measured from $\psi \to \pi^+\pi^-\pi^0$ and $\psi \to 2\pi^+2\pi^-\pi^0$ events. Curve is monte carlo calculation.

2.2 TRIGGER

The Mark II employed a two level trigger system. The primary trigger required a coincidence among (1) beam crossing, (2) pipe counter hits, and (3) hits in at least 4 of 9 drift chamber layers. The decision on a primary trigger was made in approximately 500 nsecs., which was well within the 780 nsecs. between beam crossings at SPEAR. The primary trigger rate varied from approximately 30 Hz at low beam energies to about 1 kHz at a beam energy of 3.7 GeV.

The secondary trigger was based on hardware track recognition by twenty-four microprocessors (called curvature modules[32]) working in parallel. A secondary trigger required one track giving a hit in at least 4 of the 6 axial drift chamber layers plus the corresponding TOF counter and another track giving a hit in at least 3 of the inner 5 layers of the drift chambers. This decision was made in 30 microseconds and was greater than 99% efficient for events satisfying the required topology. Since the rate of primary triggers was at most 1 kHz., the resulting dead time was at most 3%. The secondary trigger rate was 1-3 Hz. The trigger system of the Mark II is described in more detail in Reference 33.

Chapter III

EVENT SELECTION

The data used came from running at several fixed center of mass energies from 3.52 to 6.7 GeV and from scans over the region from 3.88 to 6 GeV. Table 2 summarizes the integrated luminosity accumulated at the energies used and the expected number of tau pairs produced, calculated from the theoretical cross section in section 1.2.1.

Since all tau decays produce at least one undetected neutrino, it is not possible to discover them by peaks in invariant mass spectra. Instead, one looks for an event topology which is characteristic of the decay in which one is interested and which has minimal background from other processes. There are three major distinguishing features of tau decays. First, the leptonic branching ratios are large. Electrons and muons provide a convenient tag for tau events. Second, the multiplicities are low. Most tau decays, including the leptonic decays, produce only one charged particle, which means that tau pair production primarily contributes to events with only two charged charged particles. In contrast, hadronic events at these energies have a mean multiplicity[34] of $2.1 + .8 \ln(s)$ (s is the square of the center of mass energy in GeV^2). Third, there

$\sqrt{s}$ (GeV)	Integrated Luminosity (/nb)	Number of Tau Pairs
3.52	196	0
3.67	945	1790
3.77	1991	5080
4.19	411	1400
4.42	766	2620
5.20	5200	15340
6.0,6.5,6.7	4530	9520
3.8-4.4 Scan	3310	11060
4.5-6.0 Scan	3820	11080
		58610

Table 2. Integrated luminosity and the expected number of tau pairs for the center of mass energies at which data was collected.

is always missing momentum and energy because of the neutrinos which are not detected.

It is possible to verify that events of a given topology are from tau decays by looking at some of their kinematic distributions. First, many tau decays are two body which at a fixed center of mass energy gives rise to a flat energy spectrum for the decay products. Second, the correct energy dependence of the production cross section can be checked by looking at the product of the cross section and the branching ratios as a function of the center of mass energy. Finally, when a lepton tag is used, the momentum spectra of the leptons are excellent for differentiating taus from semileptonic charm decays, the only other known source of "anomalous" leptons at SPEAR energies. The

lepton momentum spectra are checked both by the observed spectrum of the leptons and, assuming equal production of electrons and muons, by the ratio of events with an electron or muon tag since the detection efficiencies for the two have different momentum dependence. Thus, identifying a sample of tau decays consists of selecting events of the appropriate topology, measuring or calculating the background from other processes, and verifying that the kinematic properties are consistent with tau decays.

Data from the Mark II was first processed by a set of track reconstruction and measuring routines and then by vertex reconstruction routines. The charged tracking was determined from a Monte Carlo to be greater than 97% efficient over 80% of the solid angle. The radial position of the vertex was used to eliminate events where an electron or positron from the beams interacted in the vacuum pipe surrounding the beams. Cosmic ray events were eliminated by the time-of-flight system.

The decay modes measured here each produce only one charged particle and are best studied in events with exactly two oppositely charged particles (except for part of the K* analysis, which involved four charged particles). Fig. 6 shows the z position of the vertex for these events. The peak around z=0 is due to e+e- annihilations, and the flat background is from the e+ or e- beams interacting with residual gas molecules in the SPEAR vacuum region (beam-gas events). Events with a vertex at |z| greater than 10 cm

were eliminated to insure that the signal events were associated with e+e- interactions. Fig. 7 shows the difference in z of the two charged tracks at the vertex. A cut of 10 cm was applied to eliminate events with poorly measured tracks. A scan of the rejected events showed that they were primarily cosmic rays.

The acoplanarity angle is defined in two charged particle events as (180-ϕ) where ϕ is the angle between the projections in the x-y plane of the particle momenta. The QED processes e+e- → e+e-γ or $\mu^+\mu^-\gamma$ and the two photon processes e+e- → e+e-e+e-, e+e-$\mu^+\mu^-$, e+e-$\pi^+\pi^-$ (these events have four charged particles produced, but the scattered e+e- are never detected) have cross sections which are comparable to or larger than the tau production cross section, but which peak strongly at small acoplanarity angles. To reduce background from these processes, the acoplanarity angle was required to be greater than 20 degrees. This resulted in a loss of signal events ranging from 10% at a center of mass energy of 3.67 GeV to 25% at 6.5 GeV.

Computer generated pictures of the events used in the final analysis were scanned to eliminate ones with an extra charged track not found by the tracking routines and to eliminate poorly tracked cosmic ray events. Events with a neutral particle detected by the proportional chamber endcap were also eliminated (the liquid argon endcap was not used because of noise problems).

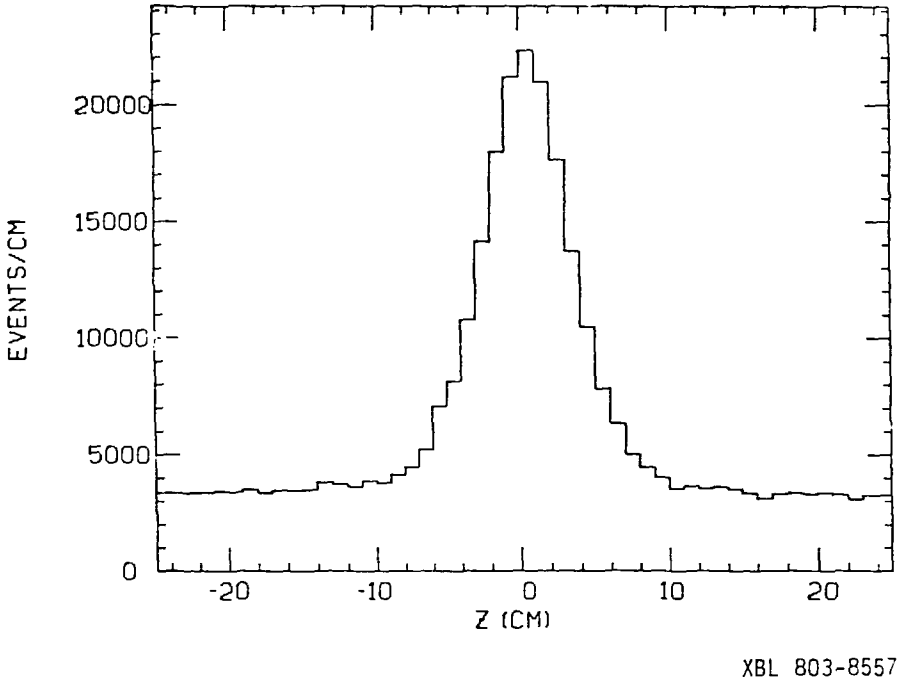

Fig. 6. Z position of the vertex for acoplanar, two charged particle events.

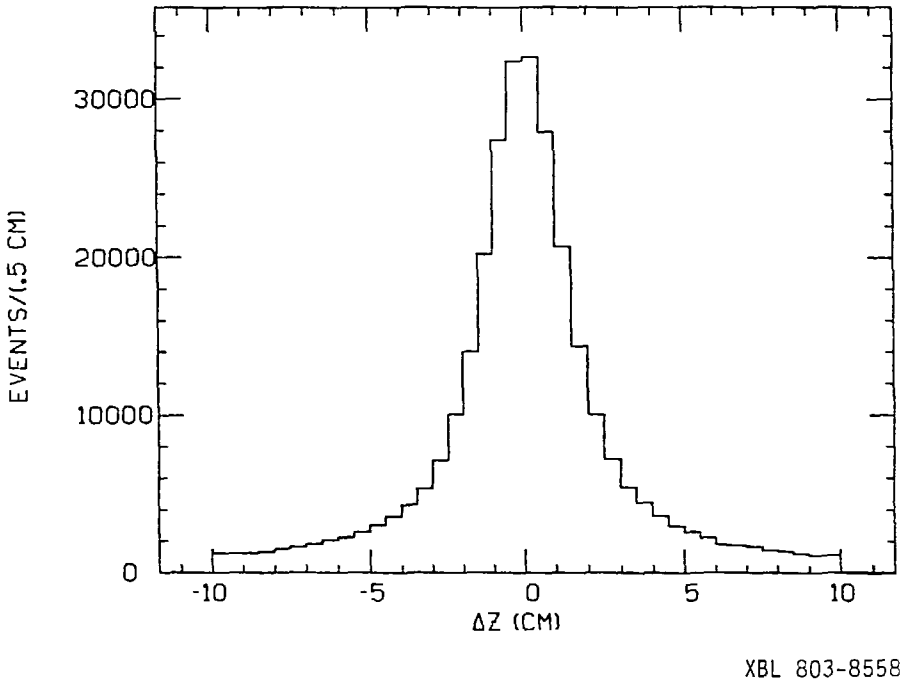

Fig. 7. Difference in z at the vertex for particles from acoplanar, two charged particle events.

Chapter IV

PARTICLE IDENTIFICATION

When looking for exclusive event topologies, it is important to identify particles correctly in order to maximize the efficiency while minimizing background from particle misidentification. This is particularly true when leptons are used as an event tag.

A particle was called a muon if there were hits in the muon system within three standard deviations of the projected track position in the number of layers expected to be reached by a muon of the particle's momentum. Fig. 7 shows the efficiency for tagging muons correctly. Pions can simulate muons by either decaying or penetrating the iron absorbers. Fig. 8 shows the combined effect of these as measured with multi-prong decays of the psi.

Above .4 GeV/c liquid argon information was used with a binary decision tree method to identify electrons. This was done by working in a multi-dimensional space spanned by a track's momentum and direction measured by the drift chambers, the total energy deposited in the liquid argon module, the energy deposited in each layer, the spatial width of the shower in each layer, and a few combinations of these variables. A recursive partitioning decision

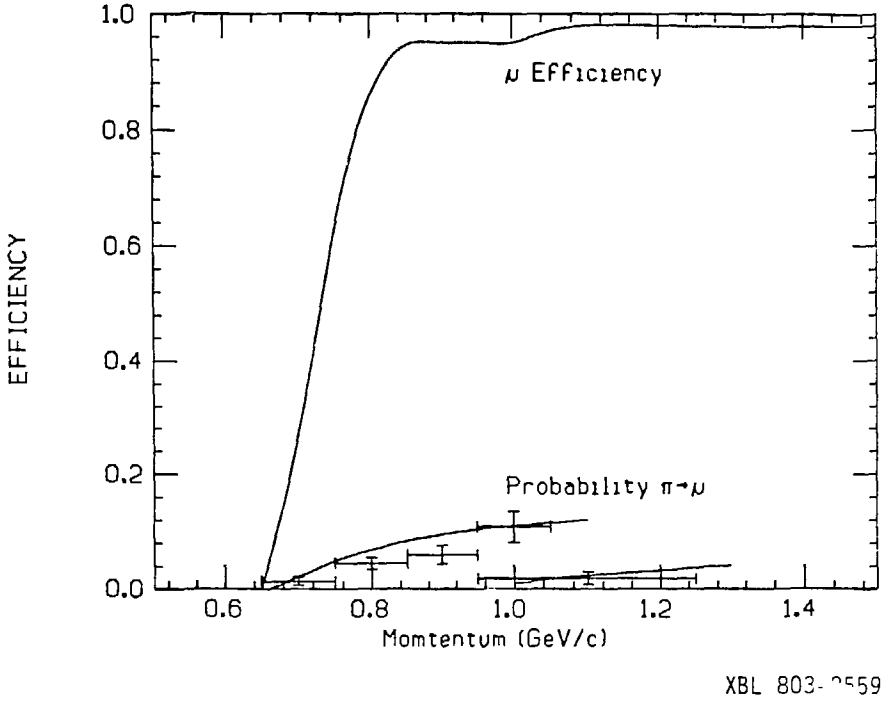

Fig. 8. Muon system efficiency excluding geometry and the pion misidentification probability. Curves are from monte carlo calculations and data points were determined from multiprong decays of the ψ.

rule[35] was used with a set of known electrons and pions to decide which hypervolumes of this multidimensional space were occupied predominantly by electrons, pions, or both (ambiguous regions). The major advantage of this method was that the a priori distributions in the space did not need to be known. The sources of known electrons were gamma conversions in the beam pipe and Bhabha events where one of the electrons had bremsstrahlunged in the beam pipe. The pions came from multi-pion decays of the psi. The efficiencies and misidentification probabilities (Figs. 9 and 10) were measured by using a separate set of known electrons and pions other than those used to build the decision trees. For a more detailed explanation of the electron-hadron separation, see Appendix B.

The TOF system was used for identifying protons and kaons. Each particle was assigned a weight to be a pion, kaon, or proton according to the gaussian probability that a pion, kaon, or proton of that momentum and flight path length would give the measured time of flight. The sum of the weights was normalized to one. A particle was called a proton if its weight for a proton was greater than .8. A particle with momentum less than 1.3 GeV/c and weight for a kaon greater than .8 was called a kaon. From the TOF resolution, the probability that a pion was called a proton was calculted to be small (less than 1% even at 2.0 GeV/c), and the probability that a kaon was called a pion had a maximum value of 4.5% at 1 Gev/c.

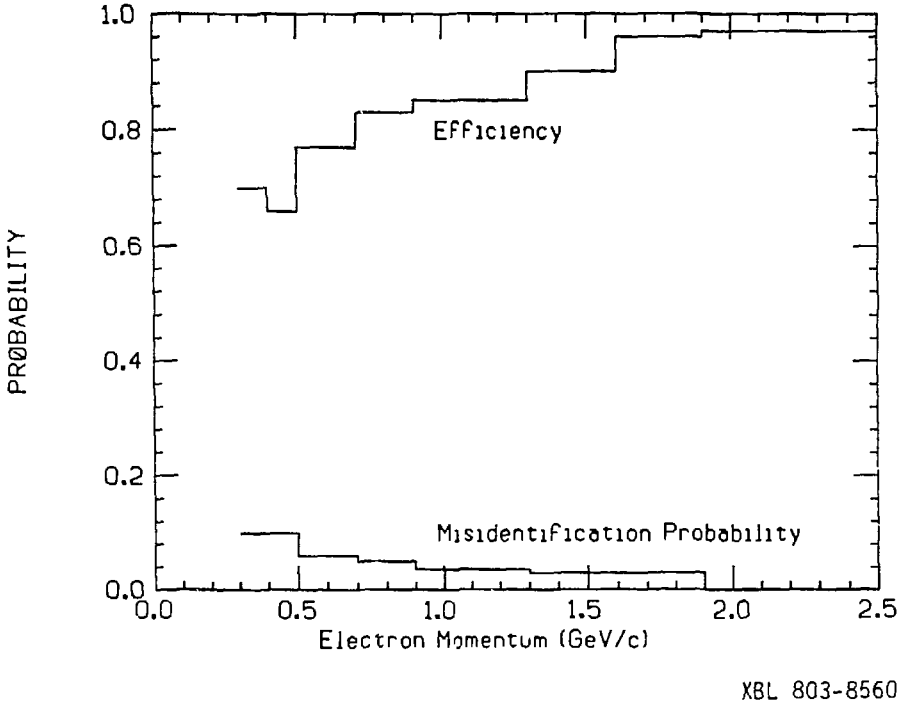

Fig. 9. Efficiency and misidentification probabilities for electrons for electron-pion separation. The sum of the efficiency and the misidentification probability is not unity because some particles are classified as ambiguous.

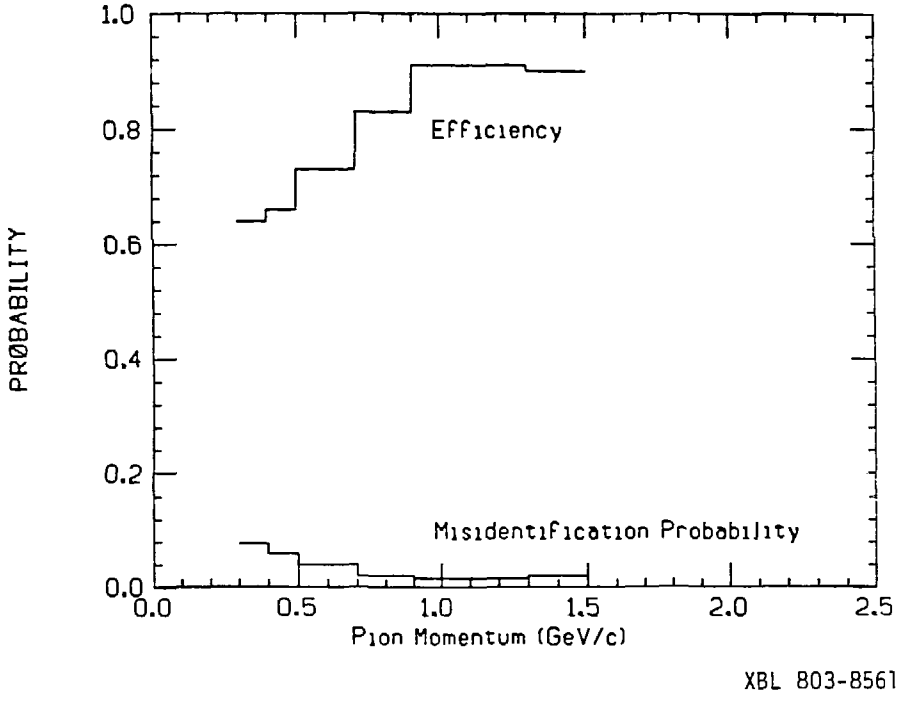

Fig. 10. Efficiency and misidentification probabilities for pions for electron-pion separation. The sum of the efficiency and misidentification probability is not unity because some particles are classified as ambiguous.

A particle was called a pion if (1) the muon system said it was not a muon without ambiguity, (2) it was not a kaon or proton according to the TOF criteria given above and (3) the e-hadron separation program said it was a hadron without ambiguity. The efficiency for identifying pions (Fig. 11) decreases below a momentum of .7 GeV/c because of the range threshold of the muon system. Any particle which could not be classified according to the above criteria was called an unknown (X).

Photons were defined as any neutral particle reconstructed in the liquid argon shower counters. Photons with energy below 100 MeV were not used. Furthermore, to reduce spurious photons (see Appendix B) formed from energy deposited by interacting charged tracks, any photon within 36 cm of a charged track at the liquid argon shower counter was not used. This distance was determined by a step in the distribution of the distance between photons and charged particles.

The gamma-gamma invariant mass for events with two charged particles is shown in Fig 12. A clear pi zero peak can be seen on top of a large, presumed combinatoric background. This background is greatly reduced by requiring that the events contain only two photons (Fig. 13). All gamma-gamma combinations with an invariant mass between 80 and 200 MeV/c^2 were included in the pi zero sample. A one constraint fit to the pi zero mass (see Appendix A) was

then done to improve the momentum resolution of the pi zeros.

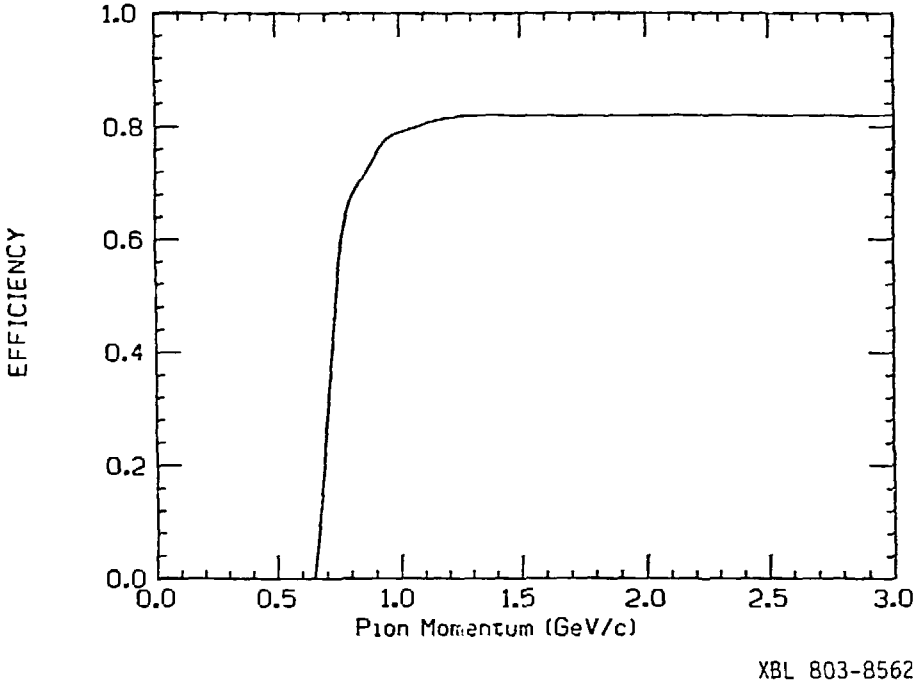

Fig. 11. Pion identification efficiency as determined by
(1) measurement of electron-pion separation,
(2) measurement of muon-pion separation, and
(3) calculation of the TOF identification probabilities, assuming a 300 psec. resolution.

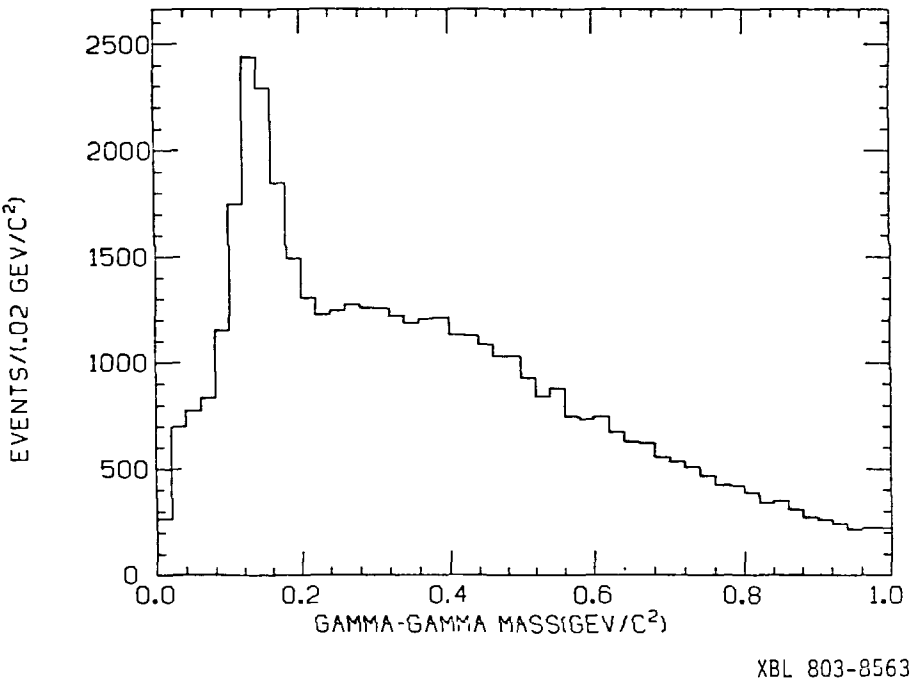

Fig. 12. Gamma-gamma invariant mass for acoplanar, two charged particle events.

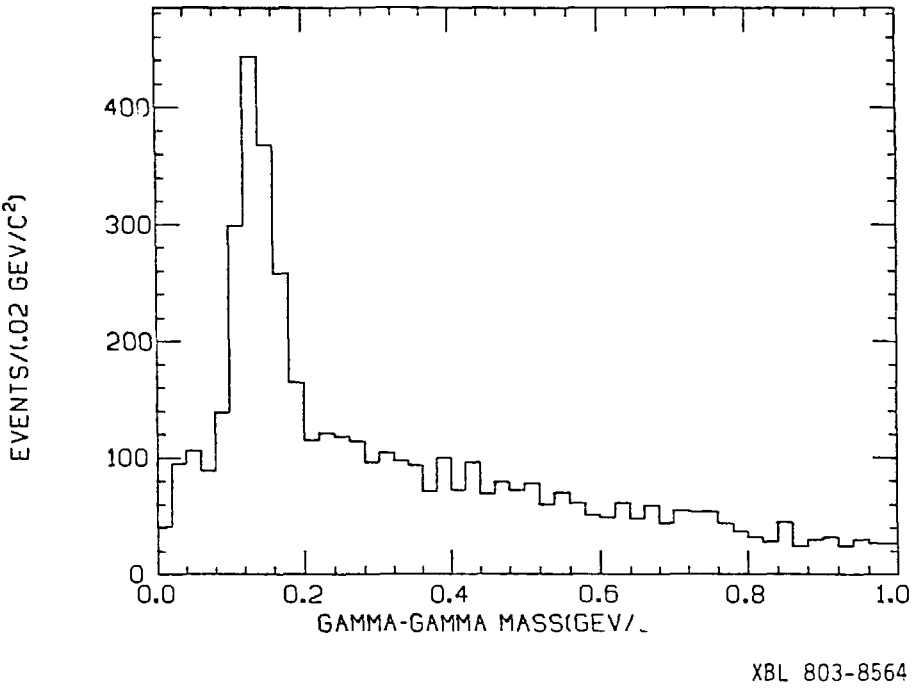

Fig. 13. Gamma-gamma invariant mass for acoplanar, two charged particle events with exactly two photons detected.

Chapter V

EFFICIENCIES AND BACKGROUNDS

5.1 EFFICIENCIES

The efficiency for detecting an event topology from tau decays was calculated from a Monte Carlo. Tau pairs were produced according to the theoretical[35] differential cross section for a pointlike, spin 1/2 particle of mass 1.782 GeV/c^2. Polarization effects and initial state radiation[36] were taken into account. The angular and momentum distributions of the decay products were determined from the theoretical differential decay widths, when known, or from phase space when the theoretical angular and momentum dependences were not known. A massless tau neutrino and a V-A coupling of the tau to the standard weak current were assumed.

The Monte Carlo then tracked each particle out through the detector geometry and generated hits in the various elements of the detector according to the measured efficiencies and resolutions. The measured magnetic field, multiple scattering, dE/dx losses, nuclear interactions, bremsstrahlung of electrons, photon conversions, pion penetration of the muon system, and particle decays were included. In order to obtain efficiencies as a function of

the center of mass energy, they were determined at several points, and polynomial fits were done.

Since all event topologies used were required to have a specific number of photons detected, there was an inefficiency due to spurious photons ("photons" formed from electronic noise (see Appendix B)). This rate was measured by looking at types of events that should have few or no real photons in them and measuring the rate at which photons were found. Since spurious photons could be formed by electronic noise combining with energy deposited by real particles, the rate of spurious photons depended on the number of particles in the event. Thus it was necessary to select events to measure the correction that had the same number of particles as signal events. For events with two charged particles and no photons produced, mu pair events ($e^+e^- \rightarrow \mu^+\mu^-$) were used. The average correction was 6% and was as large as 12% for some of the data. This was checked by using cosmic ray and Bhabha events. After correcting for the number of real radiated photons in Bhabha events that passed the cuts (about 3% of the events), the spurious photon rate for mu pairs, cosmic rays, and Bhabhas agreed within 1%. Hence a 1% systematic error was assigned to this correction.

Using the detailed shower Monte Carlo EGS[31] it was found that 4% of the real photons had an extra spurious photon associated with them. This was checked in the data

by using the three pion decay of the psi ($\psi \rightarrow \pi^+\pi^-\pi^0$). In 13 $\pm$ 2% of these events, at least one extra photon with energy greater than 100 MeV and at least 36 cm from a charged track was found. The expected number was 6% determined from mu pairs in the same data plus 4% for each of the two real photons, for a total of 14% of the events. Since this correction was not measured directly in the data used, a 5% systematic error was assigned to it.

Some high momentum pi-zeros were lost because the opening angle of the two photons was too small for them to be resolved by the liquid argon system. This was a small effect since the flight path was large (1.8 m) and the strips in the liquid argon modules were narrow (3.8 cm). Using the shower Monte Carlo EGS, it was found that 5% of the pi-zeros at 1.5 GeV/c and 10% at 2 GeV/c were lost due to this effect. The correction for this loss was calculated by folding these numbers with the observed pi-zero spectrum.

5.2 BACKGROUNDS

5.2.1 Tau production

The largest backgrounds to tau decays are other tau decay modes. These were calculated by the same Monte Carlo and tau production model described in Section 5.1. Each tau was decayed according to a combination of experimentally measured branching ratios (for $e\nu\nu$, $\mu\nu\nu$, $\pi\nu$, $\rho\nu$, $A_1\nu$,

and $K^*\nu$) and theoretically predicted branching ratios (for $\geq 4\pi\nu$ and $K\nu$). These backgrounds ranged from 10% in e-mu events (Chapter VI) to 30% in pi-X events (Chapter VIII).

A 20% uncertainty due to uncertainties in the Monte Carlo was assigned to all backgrounds from taus. In addition, the uncertainties in the branching ratios (50% for theoretical values) and uncertainties due to limited statistics were folded in.

5.2.2 QED processes

The QED processes that lead to two acoplanar, charged tracks detected are radiative Bhabhas[37] ($e^+e^- \rightarrow e^+e^-\gamma$), radiative mu pairs[38] ($e^+e^- \rightarrow \mu^+\mu^-\gamma$), and the two photon creation of electron, muon, or pion pairs[39] ($e^+e^- \rightarrow e^+e^-e^+e^-$, $e^+e^-\mu^+\mu^-$, or $e^+e^-\pi^+\pi^-$). The two photon events have four charged particles in the final state, but the electron and positron are scattered at small angles to their initial directions and are not detected.

The differential cross section for all these reactions except $e^+e^- \rightarrow e^+e^-\pi^+\pi^-$ can be calculated exactly. For $e^+e^- \rightarrow e^+e^-\pi^+\pi^-$ there are unknown form factors of the pion; pointlike pions were assumed. The backgrounds were determined by numerically integrating the differential cross section folded with the appropriate particle detection efficiencies and identification or misidentification probabilities. The limits of integration were determined by the

detector geometry and the event selection criteria. The backgrounds from QED processes were less than 5% in all cases. For uncertainties in the particle identification and misidentification probabilities and in the numerical integration, a 20% error was assigned to these calculations.

5.2.3 Hadronic production

Backgrounds from events with four or more charged particles produced were measured by looking at events which met all of the event selection criteria except that the two detected charged particles had the same charge. Assuming that the probability of missing two charged particles was independent of the their charges, the number of background events was twice the number of events with two particles of the same charge.[40] This was at most a 4% subtraction.

Backgrounds from hadronic production of only two charged particles and any number of neutral particles were calculated as described below from an all-pion jet model and a charm production model.

5.2.3.1 Old physics

To estimate the background from hadron production not associated with charm, an all-pion jet model was used. The inputs to the model were the mean charged particle multiplicity as measured over the SPEAR energy range and a limited

transverse momentum, again as measured. The amount of this production was assumed to be the colored-quark model prediction of two units of R. The most this contributed was 7% to the lepton-rho events (Chapter VII). An uncertainty of 25% was assigned to these backgrounds primarily because of the assumption that only pions are produced and because of uncertainties in particle identification and misidentification probabilities.

5.2.3.2 Charm production

Unfortunately, there is still much that is not known about the production and decay of D mesons; even less is known about F's and charmed baryons. To allow for this, upper and lower limits for charm backgrounds were calculated within the known properties and reasonable variations of the theoretical expectations of D's. The background was taken to be an average of the two limits and an error sufficiently large to cover both was assigned. The level of charm production was assumed to be the difference between the measured value of R and two units of R for "old physics". This was assumed to be all D production except for the measured contribution of charmed baryon production,[44] which was estimated to have negligible contribution to backgrounds here. Consideration of reasonable decays of F's indicated that they should contribute to backgrounds at rates comparable to D's. The largest uncertainty in the

background came from lack of knowledge of the number of extra pions that are produced with D pairs (either $D\bar{D}$, $D\bar{D}^*$, $D^*\bar{D}$, or $D^*\bar{D}^*$) since the extra pions decrease the probability that low multiplicity events typical of taus are produced. The lower limit to the backgrounds was calculated by assuming that D's are always produced with two pions (if kinematically allowed). The upper limits were calculated by assuming that 20% (the most consistent with the D recoil mass spectrum) of the D's were produced with no extra pions and the rest were accompanied by two extra pions. The D's were decayed according to a combination of experimental[45] and theoretical branching ratios which were adjusted to give the measured multiplicities and momentum spectra of D decays. The maximum background subtraction for charm was $10\pm5\%$ for the lepton-rho events (Chapter VII).

5.2.4 Beam-gas

Background rates from beam particles interacting with residual gas molecules in the SPEAR vacuum were measured by looking at events which met all of the event selection criteria except that the absolute value of the z position of the vertex was between 15 and 25 cm. This is well outside the region from which e+e- interactions originated (Fig. 6). The beam-gas subtraction ranged from 0 to .7%.

Chapter VI

LEPTONIC DECAYS

The most characteristic events from tau decays come from events where one tau decays to $e\nu\nu$ and the other to $\mu\nu\nu$. To look for these events, one of the charged particles was required to be an electron and the other to be a muon. It was also required that there were no other particles detected in the event. There were 294 such e-mu events in the data sample used. The electron (Fig. 14) and the muon (Fig. 15) spectra for these events agree well with that expected for tau decays plus backgrounds.

The background from other processes was estimated to be 5 ± 3 events from D decays and 30 ± 7 events from other tau decays. In addition, there was one event with an electron and a muon of the same charge; no event had an absolute value of the z position of its vertex between 15 and 25 cm. After subtracting these backgrounds, there are $256 \pm 17 \pm 8$ e-mu events. The average efficiency for detecting e-mu events, weighted by the tau production cross section and the integrated luminosity is .071. In Fig.16, the product of the cross section and the branching ratios is plotted as a function of the center of mass energy. A two parameter fit (m_τ and $B_e B_\mu$) using equation (1) for the cross section was done yielding a tau mass of $1.80 \pm .04$ GeV/c^2.

The product of the leptonic branching ratios is calculated from

$$N_{e\mu} = 2B_e B_\mu \sum_i L^i \sigma^i_{\tau\tau} \epsilon^i_{e\mu}$$

where $N_{e\mu}$ is the number of e-mu events, B_e and B_μ are the electron and muon branching ratios, $\sigma_{\tau\tau}$ is the tau production cross section corrected for initial state radiation, $\epsilon_{e\mu}$ is the detection efficiency, L is the integrated luminosity, and the sum is over the center of mass energies at which data was taken. The result is[45]

$$B_e B_\mu = .030 \pm .002 \pm .004$$

The systematic error comes from the following added in quadrature: 6% for the integrated luminosity, 5% for radiative corrections, 3% for Monte Carlo statistics in the efficiency calculation, 5% for electron tagging, 5% for muon tagging, 1% for the spurious photon correction, and 3% for the background subtraction. If it is assumed that the ratio of the muonic to electronic widths is the theoretical value of .973, then the individual branching ratios are

$$B_e = .176 \pm .006 \pm .010$$
$$B_\mu = .171 \pm .006 \pm .010.$$

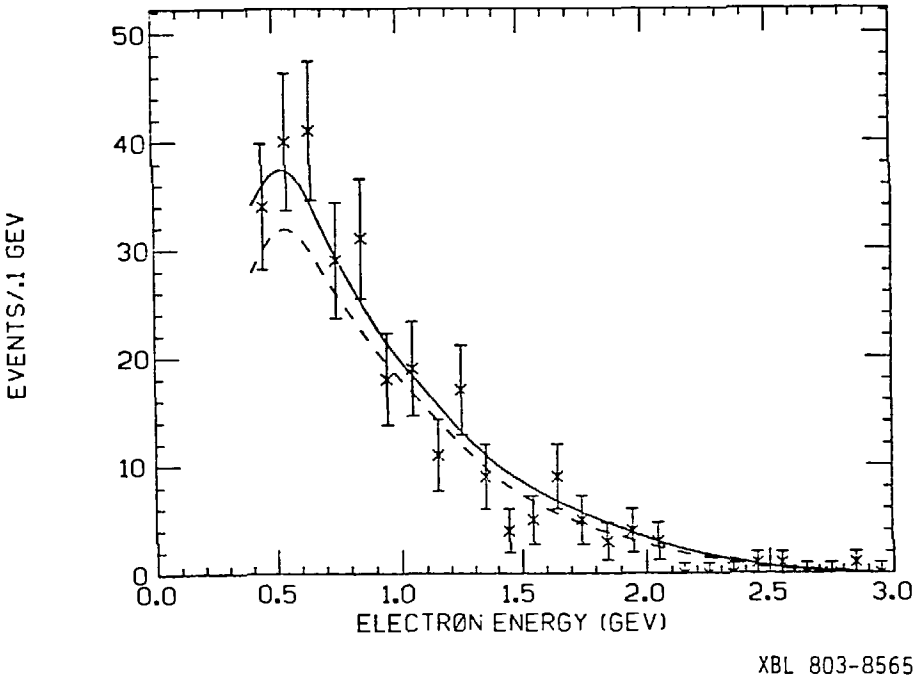

Fig. 14. Electron energy spectrum for e-μ events. Dashed curve is the monte carlo expectation for signal events. Solid curve is monte carlo expectation for signal plus background.

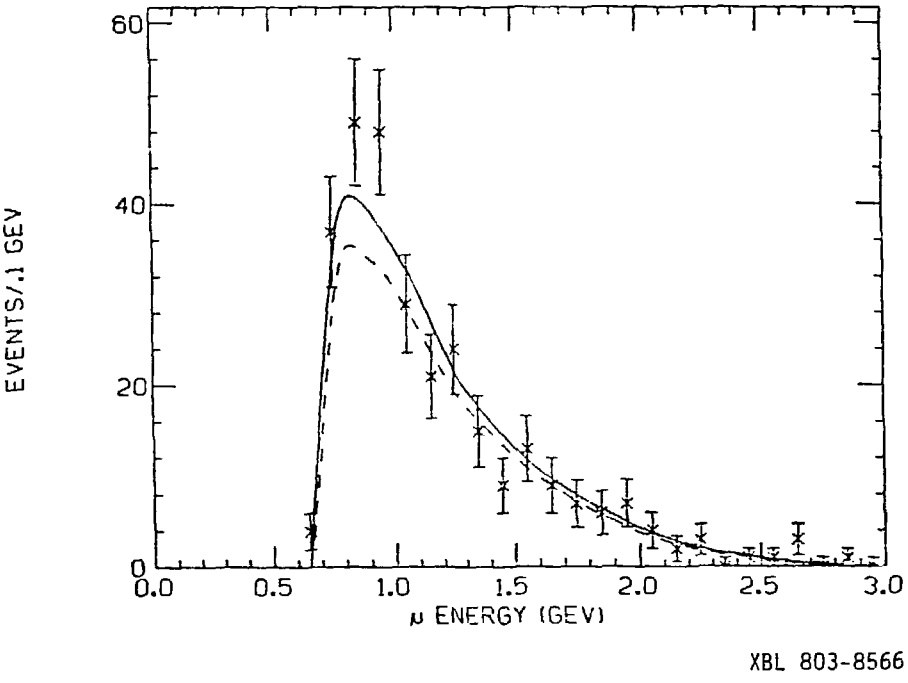

Fig. 15. Muon energy spectrum for e-μ events. Dashed curve is the monte carlo expectation for signal events. Solid curve is monte carlo expectation for signal plus background.

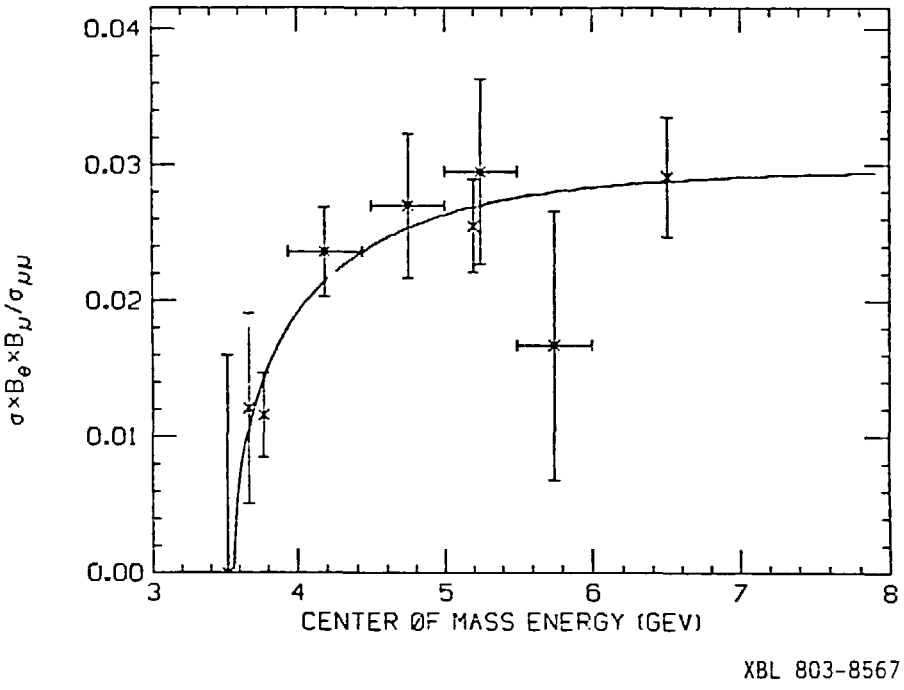

Fig. 16. Product of the tau production cross section and the leptonic branching ratios normalized to the theoretical mu-pair production cross section..

Chapter VII

TAU --> RHO NEUTRINO DECAY

To isolate events having a $\tau \rightarrow \rho\nu$ decay, further cuts were imposed in addition to the event selection criteria given in Chapter III. The rho was detected via its major decay mode $\rho^{\pm} \rightarrow \pi^{\pm}\pi^{0}$. Thus, it was required that there be a charged pion or an unidentified particle (X) in the event along with at least one pi zero. The invariant mass for all charged pions or X's with a pi zero is plotted in Fig. 17. To reduce backgrounds from gamma-gamma combinations not originating from a single pi-zero, events with more than two photons were eliminated (Fig. 18). The remaining background is primarily from the pi zero being paired with the wrong charged particle in the event. To eliminate this and to strengthen the hypothesis that these rhos came from tau decays, one of the charged particles was required to be an electron or muon. This results in a spectacularly clean sample of rhos (Fig. 19), showing that the rho dominates the two pion decay of the tau.

To verify that these lepton-rho events were from tau decays, some of their kinematic properties were checked. The muon spectrum (Fig. 20) and electron spectrum (Fig. 21) agree well with the expected curves. Fig. 22 shows the rho

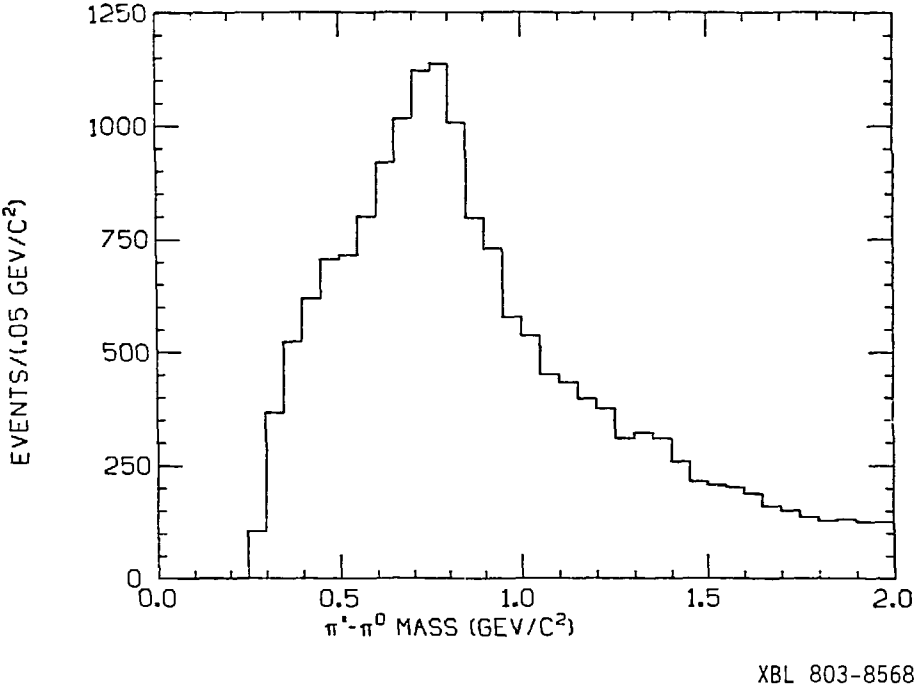

Fig. 17. $\pi^{\pm}\pi^{0}$ invariant mass for acoplanar, two charged particle events.

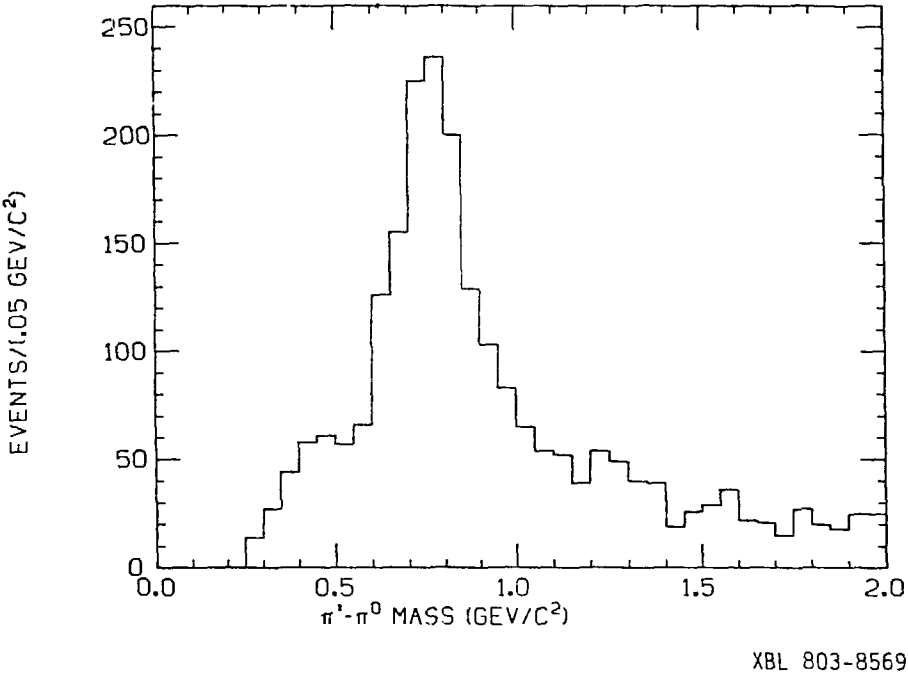

Fig. 18. $\pi^{\pm}\pi^{0}$ invariant mass for acoplanar, two charged particle events with exactly two photons detected.

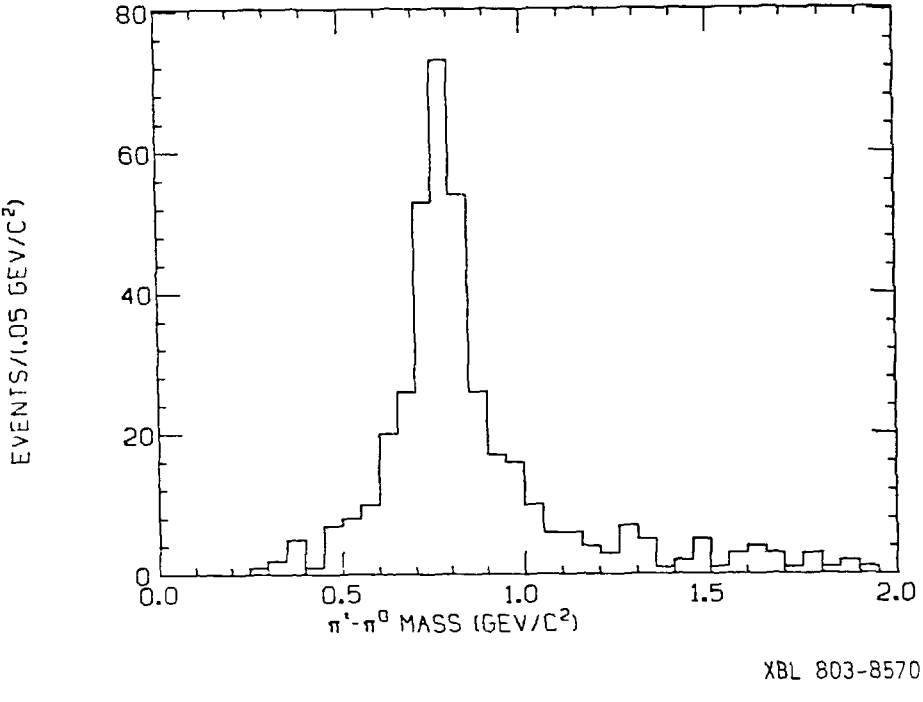

Fig. 19. $\pi^{\pm}\pi^{0}$ invariant mass for acoplanar, two charged particle events with exactly two photons detected and a lepton tag.

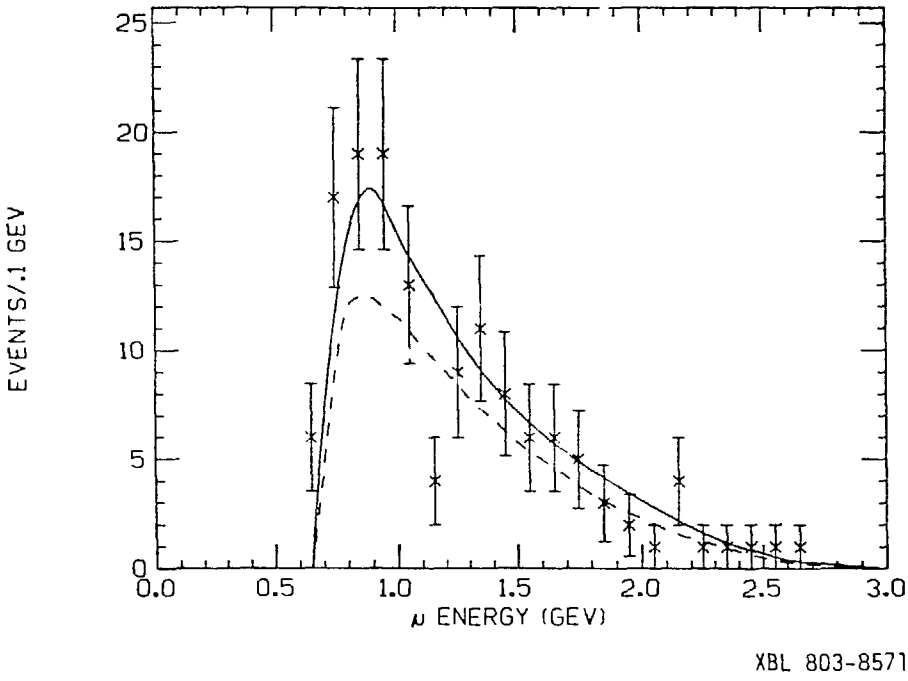

Fig. 20. Muon energy spectrum for μ-ρ events. Dashed curve is the monte carlo expectation for signal events. Solid curve is the monte carlo expectation for signal plus background.

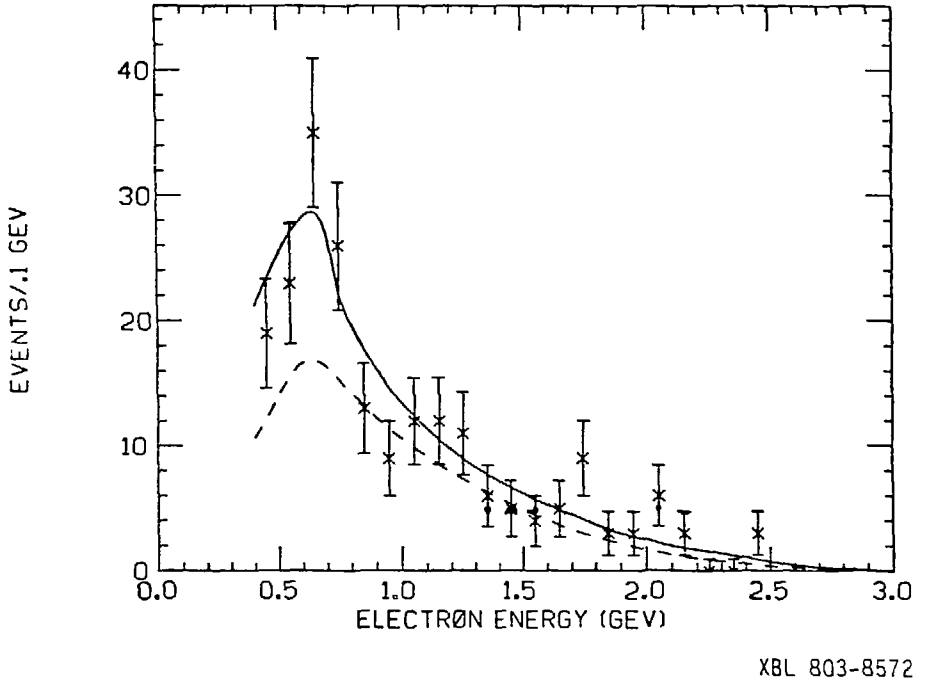

Fig. 21. Electron energy spectrum for e-ρ events. Dashed curve is the monte carlo expectation for signal events. Solid curve is the monte carlo expectation for signal plus background.

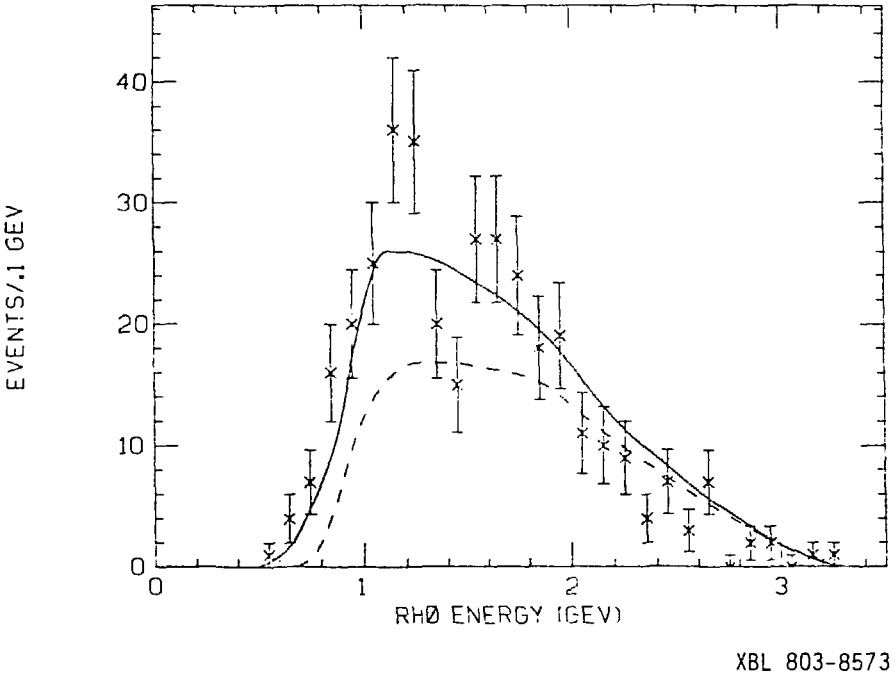

Fig. 22. ρ energy spectrum for lepton-ρ events. Dashed curve is the monte carlo expectation for signal events. Solid curve is the monte carlo expectation for signal plus background.

energy spectrum, which, if the efficiency were uniform would be a flat spectrum at a fixed center of mass energy. However, the pi zero inefficiency causes the spectrum to fall at low rho energies and the width of the rho smears the edges of the distribution. The curve is the Monte Carlo prediction which includes these effects.

In order to compare the result with Gilman and Miller[20], a rho was defined to be any $\pi^{\pm}\pi^{0}$ combination with an invariant mass less than 1.25 GeV/c^2. There were 214 electron-rho and 137 mu-rho events. In addition, there were two electron-rho events where the particles had the same charge. The backgrounds were calculated to be 10 $\pm$ 3 (9 $\pm$ 2) events from old physics, 21 $\pm$ 11 (3 $\pm$ 2) events from D's, and 40 $\pm$ 14 (22 $\pm$ 8) events from other tau decays for the electron(mu)-rho events. Subtracting the backgrounds, there is a net of 139 $\pm$ 15 $\pm$ 18 electron-rho and 103 $\pm$ 11 $\pm$ 8 mu-rho events. Combining these numbers with the average efficiencies (.034 for electron-rho and .021 for muon-rho) gives the following products of branching ratios:

$$B_e B_\rho = .034 \pm .004 \pm .007$$
$$B_\mu B_\rho = .041 \pm .005 \pm .007.$$

The systematic errors consist of the following added in quadrature: 6% for the integrated luminosity, 12% (8%) for uncertainties in the electron(muon)-rho backgrounds, 5% for Monte Carlo statistics in calculating the efficiences, 5%

for electron tagging, 5% for muon tagging, 5% for radiative corrections of the tau production cross section, 10% for the photon detection efficiencies, and 5% for the spurious photon correction. Note that some of these systematic errors partially or fully cancel in the calculations of the quantities below. B_eB_ρ and $B_\mu B_\rho$ were combined with the measured value of B_eB_μ from Chapter VI to give

$$B_e = .158 \pm .013 \pm .014$$
$$B_\mu = .190 \pm .016 \pm .021$$
$$B_\rho = .216 \pm .018 \pm .032$$
$$B_\rho/B_e = 1.37 \pm .18 \pm .24$$
$$B_\mu/B_e = 1.20 \pm .18 \pm .23.$$

Within the errors, the ratio B_μ/B_e is equal to the theoretical value of .973. Setting this ratio equal to this, the final results are:

$$B_\rho = .213 \pm .017 \pm .032$$
$$B_\rho/B_e = 1.21 \pm .12 \pm .20.$$

Plotting $\sigma_{\tau\tau}B_\rho(B_e+B_\mu)$ for the various energies at which data was collected verifies that these lepton-rho events have the correct energy dependence to be from taus. The result is shown in Fig. 23 with a curve obtained by fitting the theoretical tau production cross section times a constant. The fit gives a tau mass of $1.79 \pm .04$ GeV/c^2.

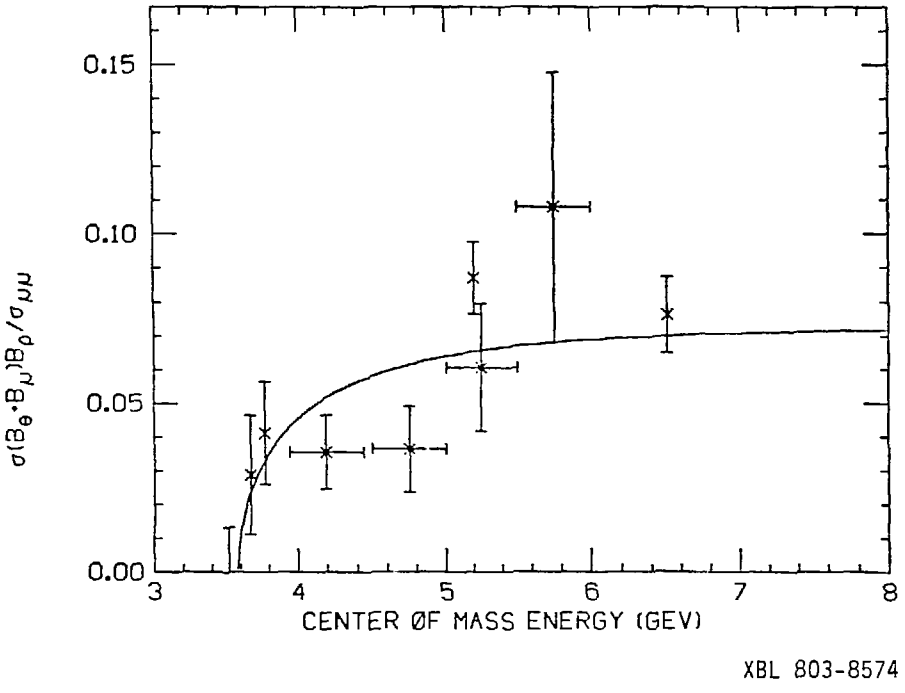

Fig. 23. Product of the tau production cross section normalized to the theoretical mu-pair cross section, the ρ branching ratio, and the sum of the leptonic branching ratios.

Chapter VIII

TAU --> PI NEUTRINO DECAY

Initial experiments[24] indicated that the branching ratio for the $\tau \to \pi\nu$ decay was significantly lower than the unambiguous prediction of the conventional model of the tau. Later experiments[25 26 27 28] indicated that this decay had the proper branching ratio, but those experiments relied on assumptions about the other decay modes of the tau. In particular, the $\tau \to \rho\nu$ decay is a major background since its branching ratio is large and the probability of missing the two photons from the pi-zero was usually relatively large in these experiments. With the measurement of the $\tau \to \rho\nu$ branching ratio in Chapter VII and with the lepton identification capabilities of the Mark II, it was possible to make a good measurement of the $\tau \to \pi\nu$ branching ratio.

For this, events were required to have one charged particle identified as a pion, a second oppositely charged particle (designated as X) which was not a kaon or proton, and no other particles in the event. There were 2150 $\pi^{\pm}X^{\mp}$ events, 40 $\pi^{\pm}X^{\mp}$ events, and 14 events with $15 < |z_{vertex}| < 25$ cm. The backgrounds were calculated to be 590 ± 170 from other tau decays (primarily $\rho\nu$ and $A_1\nu$),

49 ± 24 from charm particle decays, 97 ± 19 from old physics, 63 ± 13 from radiative bhabhas, 5 ± 1 from radiative mu pairs, and 114 ± 15 from two photon processes. This resulted in a net of 1138 ± 46 ± 174 events.

The efficiency for detecting pi-X events from taus depends on what decay mode of the tau contributed the X. Thus the number of pi-X events is given by

$$N_{\pi x} = 2B_{\pi} \sum_i \sigma^i_{\tau\tau} L^i \sum_j B_j \varepsilon^i_{\pi j}$$

where the first sum is over the center of mass energies at which data was taken and the second sum is over the decay modes of the tau. Only modes with one charged particle were used since the same sign subtraction takes care of the others. Since B_π occurs in the sum over the decay modes, this is a quadratic equation in B_π which was easily solved once $\varepsilon_{\pi\pi}$ and $\sum_{j\neq\pi} B_j \varepsilon_{\pi j}$ were determined by Monte Carlo. The average values were $\varepsilon_{\pi\pi} = .307$ and $\sum_{j\neq\pi} B_j \varepsilon_{\pi j} = .0654$ yielding

$$B_\pi = .117 \pm .004 \pm .018.$$

The systematic error consists of 15% for the background subtraction, 6% for the luminosity, 5% for initial state radiative corrections, 5% for electron-pion separation, 5% for muon-pion separation, 1% for the spurious photon correction, and 5% for uncertainties of the branching ratios in $\sum_{j\neq\pi} B_j \varepsilon_{\pi j}$. Combining this with the electronic branching ratio from Chapter VI gives

$$B_\pi/B_e = .66 \pm .03 \pm .11.$$

Fig. 24 shows the energy dependence of the product of the cross section and B_π with a fit yielding $m_\tau = 1.818 \pm .013$ GeV/c^2.

B_π was also determined by requiring that the second particle in the event be either an electron or a muon. This gave information about the leptonic branching ratios and confirmed the result from the pi-X events. The spectra of the electrons and muons accompanying the pions are shown in Figs. 25 and 26 along with the expected curves. Again, the agreement is good. There were 372 (231) e-pi (mu-pi) events of which 168 ± 29 (77 ± 15) were calculated to be background. The average efficiency for detecting e-pi (mu-pi) events was .0955 (.0542) which gives

$$B_e B_\pi = .018 \pm .002 \pm .004$$

$$B_\mu B_\pi = .024 \pm .002 \pm .006$$

$$B_\mu / B_e = 1.33 \pm .18 \pm .36.$$

Combining these with the results of Chapter VI gives

$$B_e = .150 \pm .011 \pm .021$$

$$B_\mu = .200 \pm .015 \pm .028$$

$$B_\pi = .121 \pm .009 \pm .017$$

$$B_\pi / B_e = .81 \pm .10 \pm .16.$$

Again B_μ / B_e is consistent with the theoretical value .973. Setting B_μ / B_e equal to .973 gives

$$B_\pi = .119 \pm .009 \pm .020$$

$$B_\tau / B_e = .68 \pm .07 \pm .10.$$

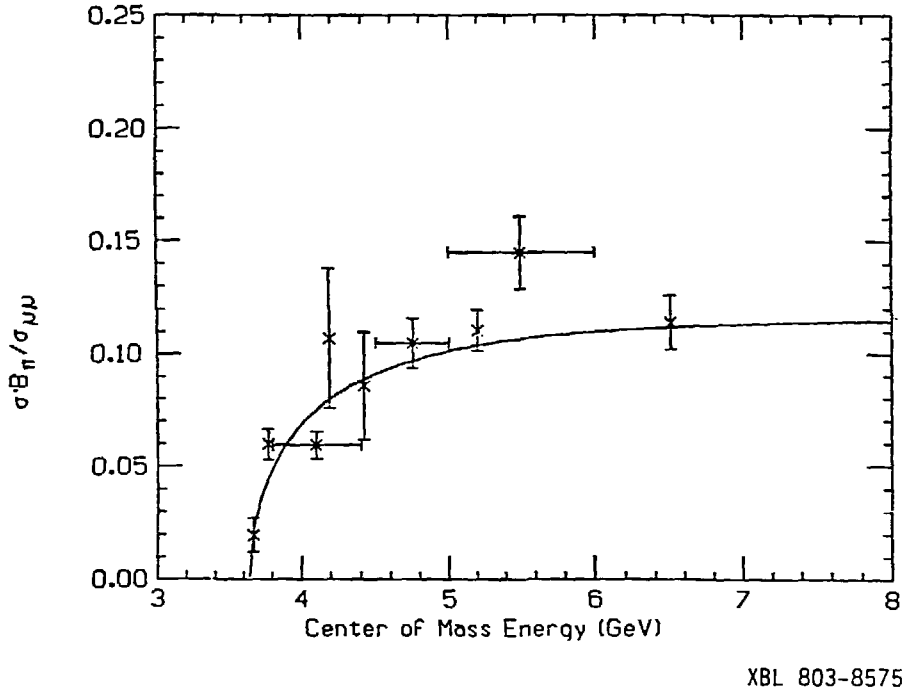

Fig. 24. Product of the tau production cross section and the pion branching ratio normalized to the theoretical mu-pair cross section.

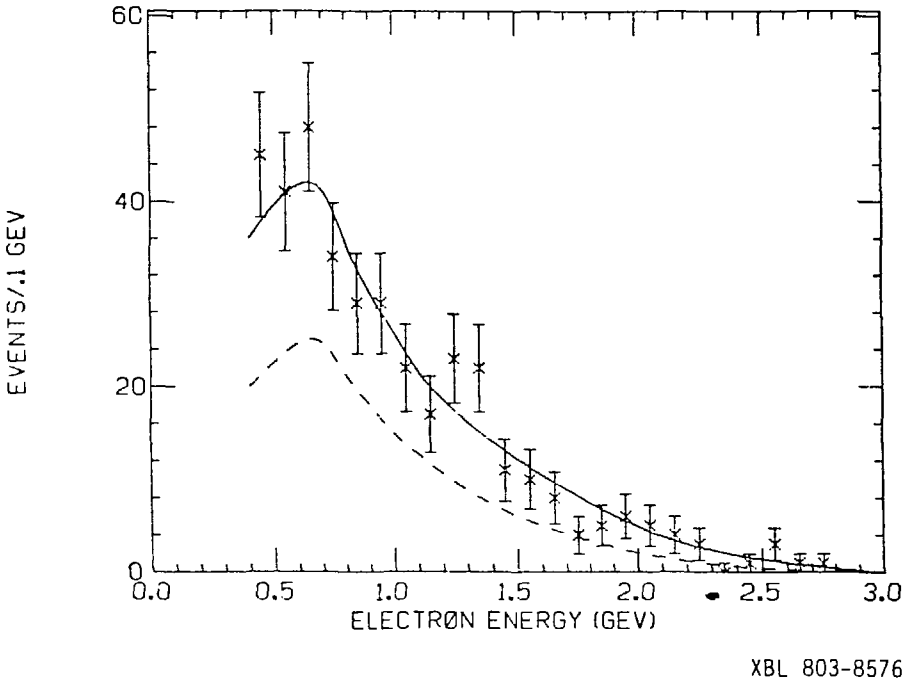

Fig. 25. Electron energy spectrum for e-π events. Dashed curve is the monte carlo expectation for signal events. Solid curve is the monte carlo expectation for signal plus background.

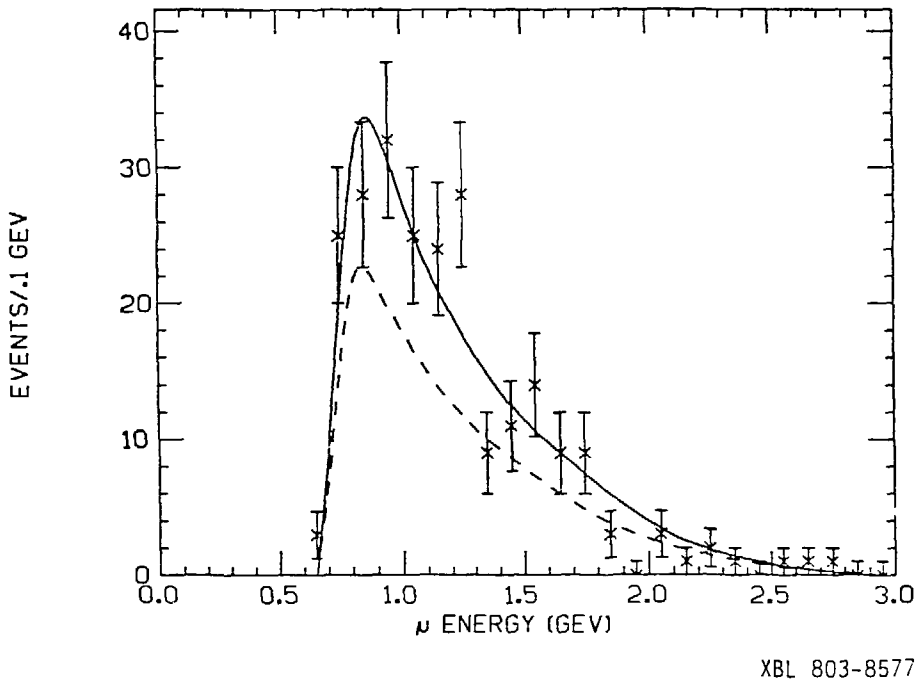

Fig. 26. Muon energy spectrum for μ-π events. Dashed curve is the monte carlo expectation for signal events. Solid curve is the monte carlo expectation for signal plus background.

Since $\tau \to \pi\nu$ is a two body decay, the energy spectrum of the pions would be flat for mono-energetic taus, that is, at a fixed e+e- center of mass energy. The upper and lower edges (E_π) of the spectrum depend on the mass of the tau, the mass of the tau neutrino, and the center of mass energy and are given by

$$E_\pi = \gamma_\tau (E^* \pm \beta_\tau p^*)$$

where p^* and E^* are the pion momentum and energy in the tau frame, given by

$$p^* = \sqrt{\frac{m_\tau^4 + m_\pi^4 + m_\nu^4 - 2m_\tau^2 m_\pi^2 - 2m_\tau^2 m_\nu^2 - 2m_\pi^2 m_\nu^2}{4m_\tau^2}}$$

This allows a determination of the tau mass or the tau neutrino mass by fitting the observed pion energy spectrum. Since the data came from many center of mass energies, the expected pion spectrum is a sum of several flat spectra. Fig. 27 shows the pion energy spectrua for various center of mass energies after bin by bin background subtractions and efficiency corrections were made. Two fits were done. The efficiency for detecting pi-X events depends on the tau mass and tau neutrino mass. This causes the fits to be sensitive to systematic variations in the efficiencies and background subtraction between data from different center of mass energies. To avoid this, only data from the largest block of fixed energy running ($\sqrt{s}$ = 5.2 GeV) was used

in the fits. First, the neutrino mass was fixed at zero and a two parameter (the tau mass and B_π) fit was done yielding $m_\tau = 1.80 \pm .04$ GeV/c^2. Second, the tau mass was fixed and the neutrino mass and B_π were varied. The neutrino mass is consistent with being zero, and Fig. 28 shows the resulting upper limit (95% confidence level) on the neutrino mass as function of the tau mass assumed. For a tau mass of 1.782 GeV/c^2, the upper limit on the neutrino mass is 245 MeV/c^2.

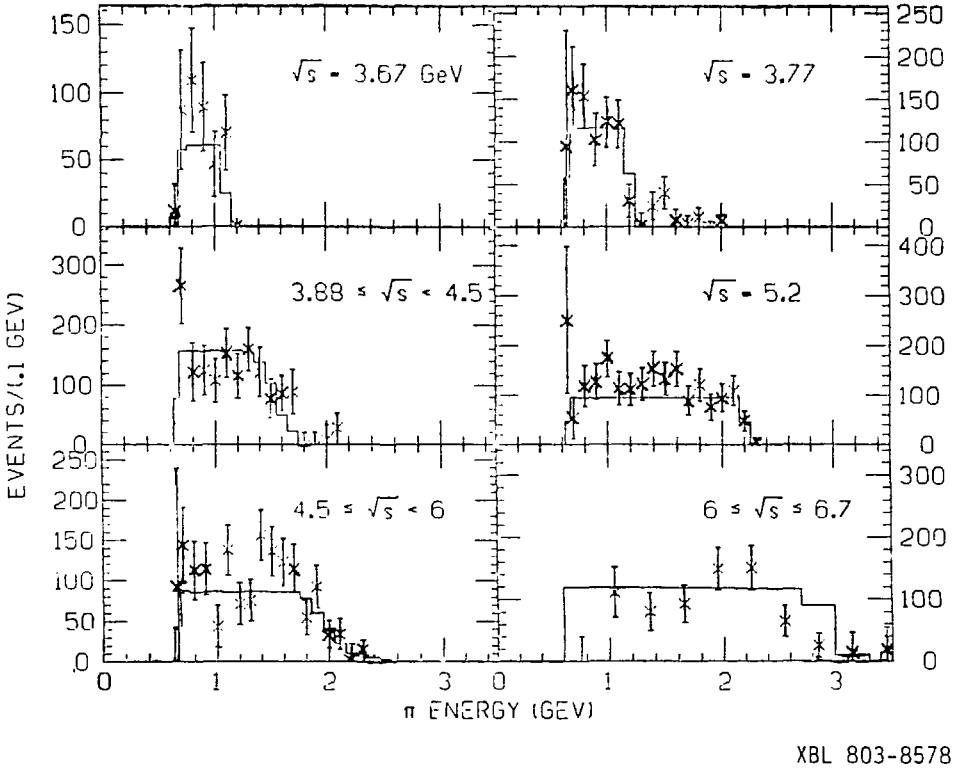

Fig. 27. Pion energy spectrum for π-X events with bin by bin background subtraction and efficiency corrections. The curves are the expected spectra for m_c = 1.782 GeV/c^2, m_u = 0, and B_π = .117.

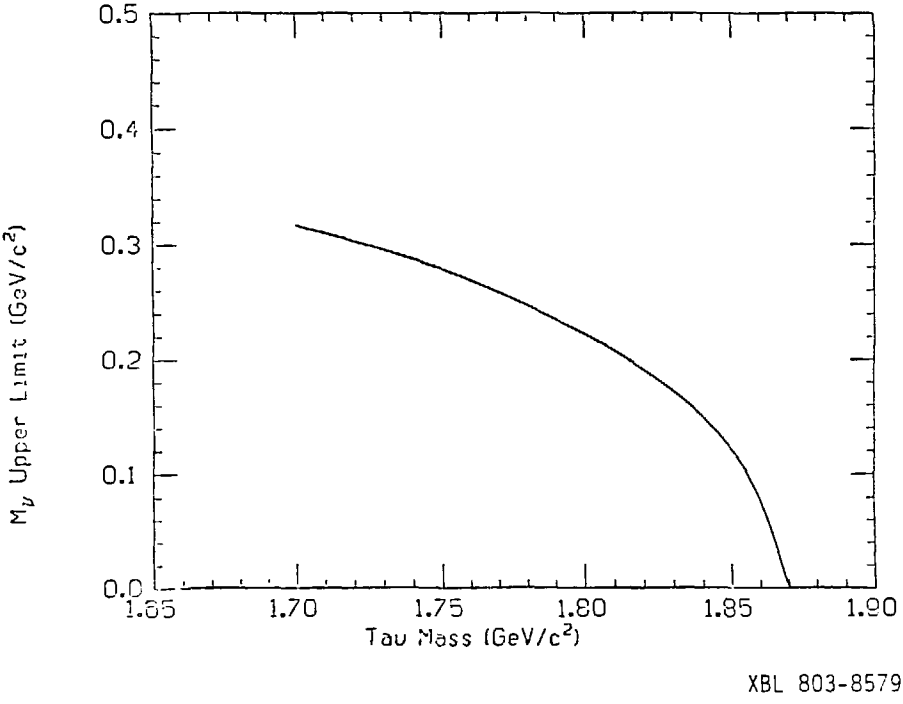

Fig. 28. Upper limit (95% confidence level) on the mass of the tau neutrino as a function of the mass of the tau.

Chapter IX

TAU --> K* NEUTRINO DECAY

If the tau couples to the conventional weak current, it should have Cabibbo suppressed decays to states containing the strange quark. Two expected decays[19] are $\tau \to K\nu$ and $\tau \to K^*\nu$, the counterparts to $\tau \to \pi\nu$ and $\tau \to \rho\nu$, respectively. This chapter contains evidence for the $K^*\nu$ mode.

9.1 SIGNAL

The $K^{*\pm}$ decays 1/3 of the time to $K_L\pi^\pm$, 1/3 to $K_S\pi^\pm$, and 1/3 to $K^\pm\pi^0$. The Mark II detector did not detect K_L's, so only the $K_S\pi^\pm$ and $K^\pm\pi^0$ modes were studied. For this analysis, only events taken at center of mass energies above 4.2 GeV were used in order to avoid the peaks in charmed particle yields below that. For the $K_S\pi^\pm$ mode, events were required to have exactly four charged particles with zero total charge and no photons. Three of the particles were required to be identified as pions or unidentified, henceforth all referred to as pions. The fourth was required to be an electron or muon as a tag of the other tau in the event. Two of the pions were identified as coming from a K_S by requiring that their invariant mass be consistent with a K_S and that they form a secondary vertex at least .2 cm in

the x-y plane (R_{xy}) from the e+e- annihilation point. A one contraint fit to the K^0 mass was done and the chi square of the fit (Fig. 29) was required to be less than 5. The resulting $K_s\pi^{\mp}$ mass spectrum (Fig. 30) has a peak at the K*(892) mass. In order to reduce the backgrounds and further insure that the K^0's were genuine, the secondary vertex was required to be at least 1 cm from the e+e- annihilation point (Fig. 31) and these events were used in the subsequent analysis. It is difficult to estimate the signal and background when dealing with low statistics and a broad resonance such as the K*. The procedure used was to define the signal bins to be the five bins from .825 to .95 GeV/c^2 and the background control bins as the ones from .7 to 1.25 GeV/c^2 exclusive of the signal bins. For the signal region, let n_s be the number of bins, N_s be the number of events found, and P_s be the probability that a K* has a mass in the that region. Let n_B, N_B, and P_B be the corresponding quantities for the background regions. Finally, let N_{K*} be the total number of actual K*'s detected and A be the number of background events per bin assuming the background is flat. Then, the following relationships are obtained:

$$N_s = P_s N_{K*} + n_s A$$
$$N_B = P_B N_{K*} + n_B A.$$

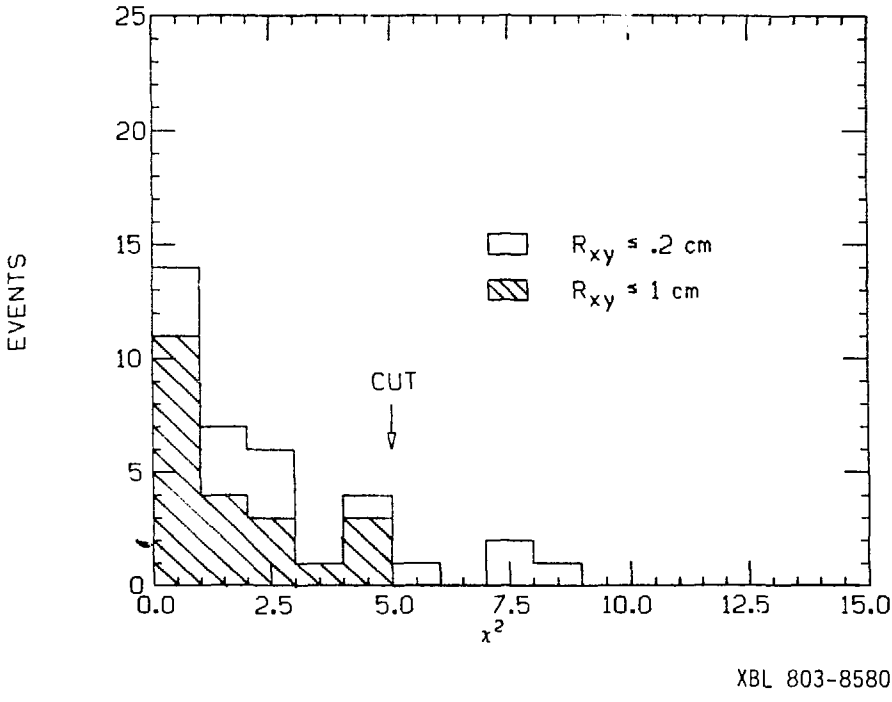

Fig. 29. Chi square of fit to the K^0 mass.

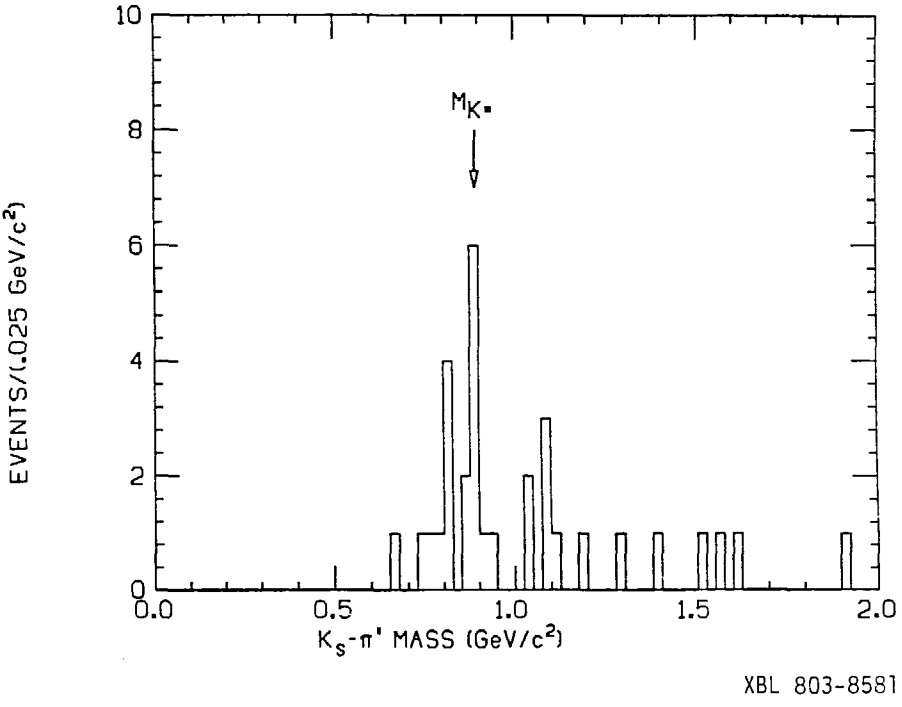

Fig. 30. K_S-$\pi^{\pm}$ invariant mass for events with a lepton tag and a K_S vertex at least .2 cm from the e^+e^- annihilation point.

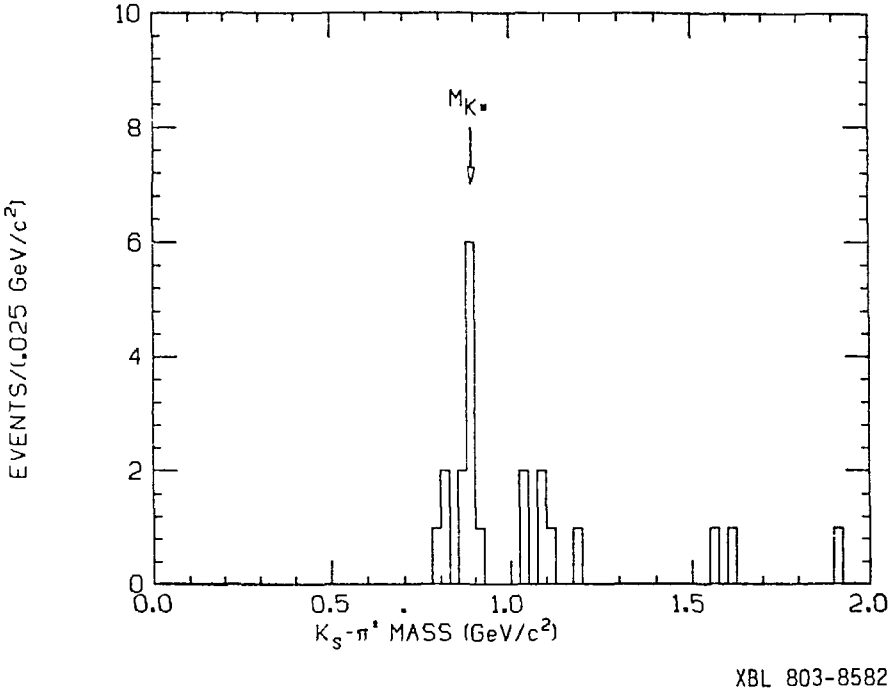

Fig. 31. K_S-$\pi^\pm$ invariant mass for events with a lepton tag and a K_S vertex at least 1 cm from the e^+e^- annihilation point.

These equations were solved for N_{K*}. Using $n_s = 5$, $n_B = 17$, $P_s = .80$, $P_B = .20$, $N_s = 9$, and $N_B = 9$ gives $P_s N_{K*} = 7 \pm 3$.

For the $K^{\pm}\pi^0$ mode, events were required to have a $K^{\pm}$, a pi-zero, a lepton as a tag, and no other detected particles. Due to the inefficiency in detecting pi-zeros, fewer events were expected than for the $K_s\pi^{\pm}$ mode, and the pi-zero resolution widened the peak. The net result was that for 7 ± 3 events from the $K_s\pi^{\pm}$ mode, 2 ± 1 events were expected from the $K^{\pm}\pi^0$ mode where the mass of the $K^{\pm}\pi^0$ was between .8 and 1 GeV/c^2. Fig. 32 shows that there were 4 events in this region and no events in the surrouding background region. This was not statistically significant by itself, but gives strong support to the $K_s\pi^{\pm}$ mode.

9.2 D BACKGROUND

Since D decays have both anomalous leptons and large strange particle content, it is imperative to show that they were not the source of these lepton-K* events. This was done by making two assumptions: (1) The K* peaks were actually K*'s and not fluctuations in the K-pi mass spectrum (the statistical signifance of the total peak is large) and (2) the lepton-K* events had only two charged particles produced, that is, there were no charged particles missed (the justification for this was that there were no $K^{\pm}K^{*\pm}$ events). First consider Cabibbo allowed decays. Since $D^{\pm}$

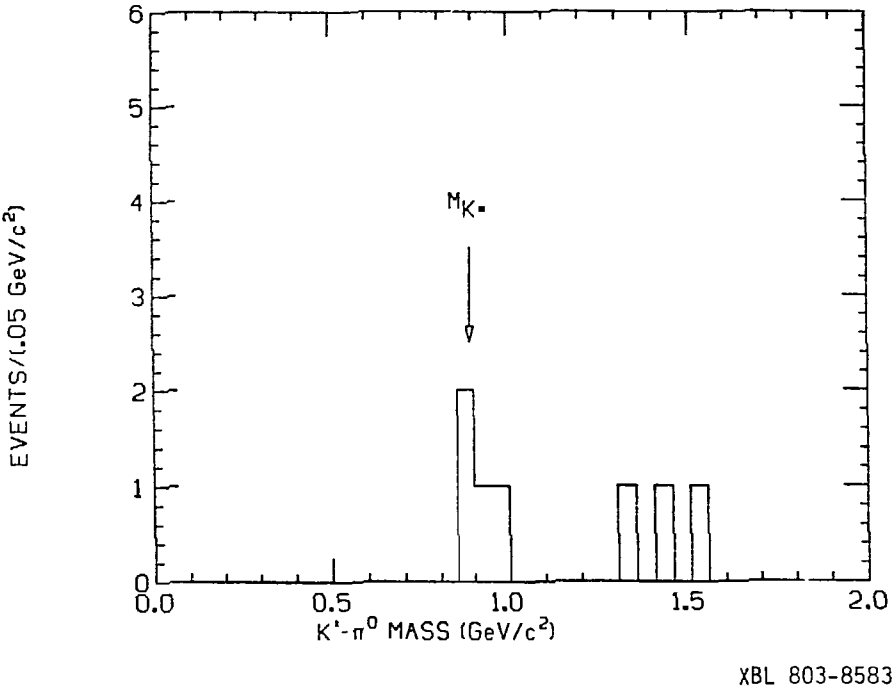

Fig. 32. $K^{\pm}$-π^0 invariant mass for events with a lepton tag.

cannot decay to K^{*-} + neutrals (it violates the $\Delta C = \Delta S$ rule), decays of charged D's cannot be the source of the lepton-K* events by assumption (2). In order to have D^0's give lepton-K* events consistent with assumption (2), it is necessary that the event contained a $D^0(\overline{D^0})$ that decays to $\ell^- + K^{*-}$ + neutrals and a $\overline{D^0}(D^0)$ that decays to all neutrals. This possibility was eliminated immediately by the fact that in 11 of the 13 events in the signal region the invariant mass of the lepton and K* was greater than the D^0 mass and the mass of the remaining two events was greater than 1.6 GeV/c^2. A Monte Carlo calculation confirmed this by showing that at most .05 of the lepton-K* events could have come from D^0's. The other possibility for D^0's is that the lepton is a misidentified pion. However, the invariant mass argument still applies and the small misidentification probabilities for particles of these momenta lead to a minute estimate for this possibility. The only other possibility is events with a Cabibbo suppressed decay $D^- \to K^{*-} + K^0$ + neutrals opposite $D^- \to \ell^- + K^0$ + neutrals. Monte Carlo calculations showed that these contributed at most .01 events. The conclusion is that the lepton-K* events were not from D decays.

9.3 RESULTS

In order to compare the properties of the events with those expected from taus, the $K_S^0\pi^-$ and $K^-\pi^+$ events were

combined and are summarized in Table 3. The ratio of the number of events with a muon tag to the number with an electron tag is .9 + .5 compared to .74 expected for taus. Although the statistics are poor, the lepton energy spectrum (Fig. 33) and the K* energy spectrum (Fig. 34) are consistent with being from tau decays.

To properly get the efficiency for finding the secondary K vertex, a feature of the Monte Carlo which generated space points in the drift chambers was used. Then this Monte Carlo data was processed through the same tracking and vertexing routines that were used for the actual data. This was also done for the $K^{\pm}\pi^0$ mode to properly account for in-flight decays of the kaon. The luminosity- and cross section-weighted average efficiencies were .0168 (.0135) for the $K_S\pi^{\pm}$ mode with an electron (muon) tag and .0048 (.0025) for the $K^{\pm}\pi^0$ mode with an electron (muon) tag. Combining these efficiencies with the number of events calculated above and assuming $B_\mu = .973B_e$ gives $B_\tau B_{K^*} = .0030 \pm .0015$ for the $K_S\pi^{\pm}$ mode and $.008 \pm .005$ for the $K^{\pm}\pi^0$ mode. These two measurements agree within the large errors and give an average value of

$$B_\tau B_{K^*} = .0042 \pm .0016.$$

Combining this with the results of Chapter VI gives

$$B_{\tau^*} = .024 \pm .009$$

$$B_{K^*}/B_e = .13 \pm .05.$$

This was combined with the measurement of the rho branching ratio from Chapter VII, and after using equations (2.11) and (3.32) of Tsai[19] to correct for phase space differences, the Cabibbo angle is 19 + 3°.

Table 3. Properties of lepton-F* events.

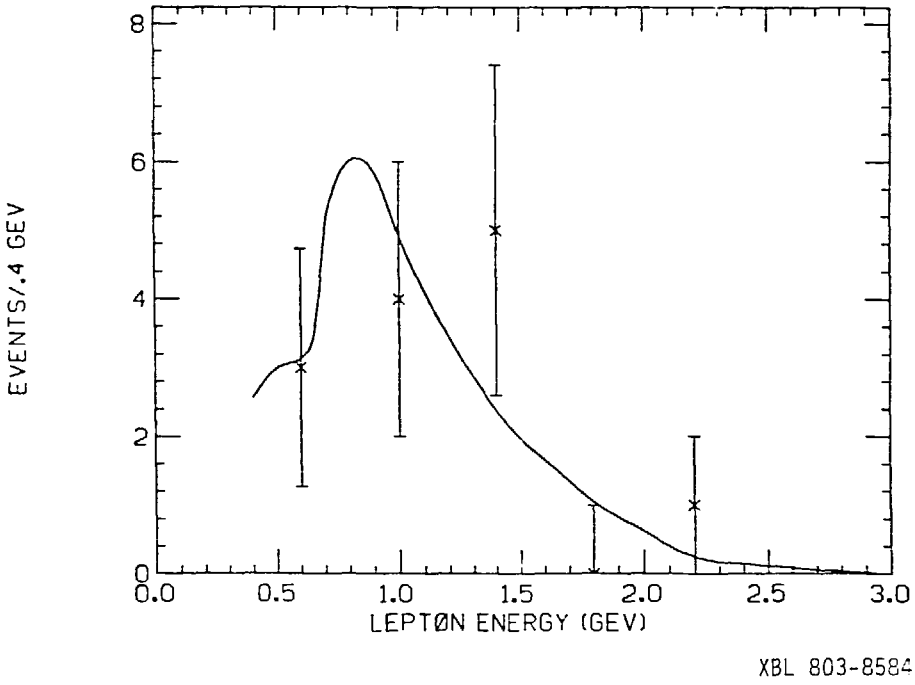

Fig. 33. Lepton energy spectrum for lepton-K* events. Curve is the monte carlo prediction.

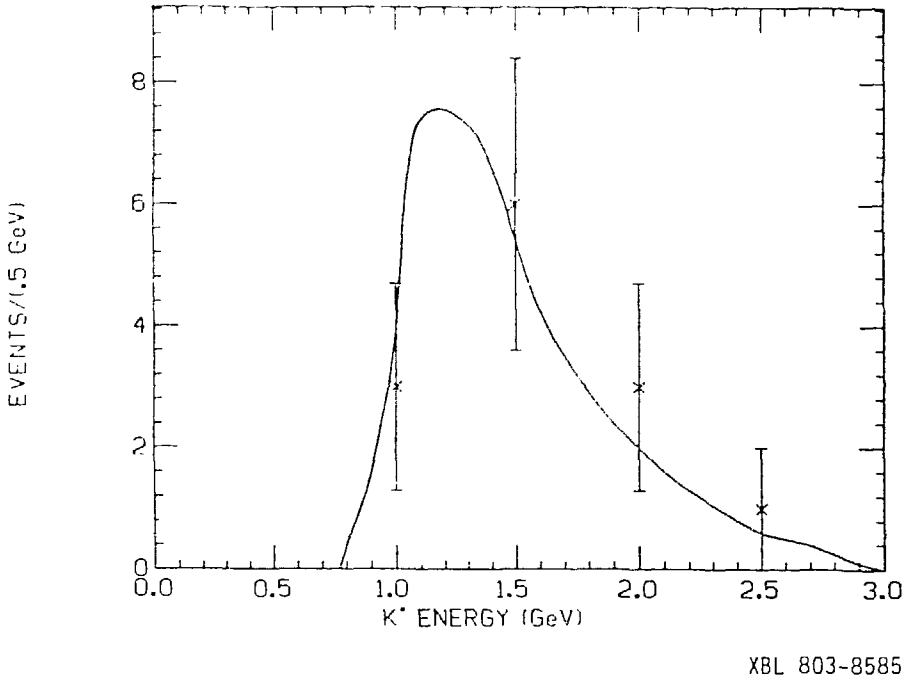

Fig. 34. K* energy spectrum for lepton-K* events. Curve is the monte carlo prediction.

Chapter X

CONCLUSIONS

Table 4 summarizes the combination of branching ratios that were measured. Since there were six measurements of the four branching ratios B_e, B_μ, B_π, and B_τ, a fit was done to determine the best values of the branching ratios. The measurement of B_π included the e-pi and mu-pi events, so to be independent B_π was recalculated without these events giving $B_\pi = .115 \pm .007 \pm .018$. Systematic errors common to all measurements, the luminosity and radiative corrections to the production cross section, were not included in the fit but were folded back in afterwards. The errors used were the remaining systematic errors folded with the statistical errors.

The results of the fit are shown in Table 5. The ratio B_μ/B_e is consistent within the errors of the theoretical value of .973. The errors on the branching fractions were reduced by constraining B_μ/B_e to the theoretical value and doing the fit again, as given in Table 5. The leptonic branching ratios agree very well with previous measurements and fortuitously well with the theoretical expectation considering the experimental error and theoretical uncertainty in the total width.

Quantity	Measured Value
$B_e B_\pi$	$.030 \pm .002 \pm .004$
$B_\mu B_\pi$	$.034 \pm .004 \pm .007$
$B_\mu B_e$	$.041 \pm .005 \pm .007$
B_π	$.117 \pm .004 \pm .013$
$B_e B_K$	$.013 \pm .002 \pm .004$
$B_\mu B_K$	$.024 \pm .002 \pm .006$
$B_\pi B_{K^*}$	$.0042 \pm .0016$

Table 4. Branching ratios measured in this experiment.

Branching Ratio	Fit Value	Fit Value $B_\pi = .973$ P
B_e(%)	15.5 ± 2.0	17.6 ± 1.1
B_μ(%)	19.4 ± 2.5	17.1 ± 1.1
B_μ/B_e	$1.25 \pm .27$	
B_ρ(%)	21.5 ± 3.4	21.4 ± 3.2
B_ρ/B_e	$1.38 \pm .28$	$1.22 \pm .18$
B_π(%)	11.7 ± 1.4	11.5 ± 1.3
B_π/B_e	$.75 \pm .13$	$.66 \pm .08$

Table 5. Final values of branching ratios found by simultaneously fitting the results in Table 4.

The ratio B_ρ/B_e also agrees extremely well with the theoretical expectation, being well within the experimental error and the theoretical uncertainty of 15%. The ratio B_π/B_e is a little higher than the theoretical prediction of .58 but is consistent with it within the errors. The pi branching ratio is higher than previous measurements, but this can be readily understood. Earlier experiments

assumed values of B_e which were too large leading to an overestimation of the feeddown to the pi's and assumed values of the leptonic branching ratios which were too large which also reduces the value of B_e obtained.

The best value of the tau mass was obtained by simultaneously fitting: B_eB_μ, $B_e(B_e+B_\mu)$, and the pi energy spectra at various center of mass energies, giving a value of $1.787 \pm .010$ GeV/c^2. This agrees with the DELCO ($1.782^{+.004}_{-.007}$), DESY-Heidleberg ($1.787^{+.010}_{-.018}$), and DASP ($1.807 \pm .020$) measurements.

In conclusion, the properties of the tau remain consistent with it being a sequential lepton coupled to the conventional weak current. The branching ratios measured here are consistent with those expected. The value of B_π/B_e shows that the axial vector current is present at the expected level. The value of B_ρ/B_e shows that the conserved vector current hypothesis is applicable to tau decays and that the vector current is present at the expected level. The value of the Cabibbo angle ($19 \pm 3^\circ$) measured from the K* decay indicates that the weak current in tau decays has the same Cabibbo structure as the ordinary weak current.

The dependence of the cross section on energy determined by e-mu (Fig. 16), lepton-rho (Fig. 23), and pi-x events (Fig. 24) verifies the spin 1/2, pointlike nature of the tau. Finally, although the upper limit on the tau

neutrino mass (245 MeV/c^2, 95% confidence level) is much higher than those for the electron and muon neutrinos, the tau neutrino is still consistent with being massless.

Appendix A

FIT TO THE PI ZERO MASS

Once a pi zero was identified, its momentum resolution was greatly improved by constraining the two photons to the pi zero mass. Fitting both the energies and the directions of the photons, although strictly the correct procedure, leads to equations that are intractable. These equations can be solved numerically for each pi zero, but that is extremely costly in computing time. Fortunately, the equations could be simplified by assuming that the energy resolution of the photons dominates their angular resolution, so that the latter may be ignored. This is a good approximation for pi zeros of energy less than two GeV.

The fit was done by defining a chi square for the photon energies and assuming the energy resolution was proportional to the square root of the energy (the actual value of the proportionality constant was irrelevant to the fit.) The chi square was then minimized with respect to the photon energies subject to the constraint that the invariant mass of the photons was the pi zero mass. The variables used in the derivation were:

$E^M_{1,2}$ = measured photon energies

$E_{1,2}$ = fit photon energies

$\sigma(E)$ = photon energy resolution = $A\sqrt{E}$

χ^2 = chi square

M_{π^0} = mass of pi zero

θ_{12} = angle between the two photons

$B = M_{\pi^0}^2/2(1-\cos\theta_{12})$.

The chi-square distribution and mass constraint are

$$\chi^2 = \frac{(E_1-E_1^M)^2}{\sigma^2(E_1)^2} + \frac{(E_2-E_2^M)^2}{\sigma^2(E_2)^2} = \frac{(E_1-E_1^M)^2}{A^2E_1} + \frac{(E_2-E_2^M)^2}{A^2E_2}$$

$$M_{\pi^0}^2 = 2E_1E_2(1-\cos\theta_{12}) \quad \Rightarrow \quad E_1E_2 = B.$$

Using equation (2) to treat E_2 as a function of E_1 and minimizing χ^2 with respect to E_1 gives

$$0 = A^2\frac{d\chi^2}{dE_1} = 1-\frac{E_1^M}{E_1^2} + \left(1-\frac{E_2^M}{E_2^2}\right)\frac{dE_2}{dE_1}$$

$$0 = 1-\frac{E_1^M}{E_1^2} - \frac{B}{E_1^2} + \frac{E_2^M}{B}.$$

The solution is

$$E_1 = \sqrt{B}\,\frac{B+E_1^M E_2^M}{B+E_2^{M2}}$$

$$E_2 = \frac{B}{E_1}.$$

Appendix F

LIQUID ARGON SYSTEM

F.1 INTRODUCTION AND CONSTRUCTION

The shower counters of the Mark II were a lead-liquid argon system of the type pioneered by Willis[F], that is, a sampling calorimeter consisting of planes of lead separated by liquid argon. Electrons and photons passing through the system showered primarily in the lead, and the ionization of the liquid argon by the shower particles was the signal collected. The system consisted of eight modules (1.5 x 3.9 x .3 m^3) in an octagonal arrangement outside the magnet coil.

Each module consisted of 37 planes of 2 mm antimony-strengthened lead separated by 3 mm gaps. Alternate planes starting with the first were solid sheets held at ground potential. The other planes were divided into 3.8 cm strips oriented at 0° (designated as F layers) or 90° (T layers) or 5.4 cm strips at 45° (U layers) to the beam direction. To reduce the amount of readout electronics necessary, strips were ganged together in depth, designated as F1 (layers 2,8), F2 (layers 14,20), F3 (layers 28,30,32,34,36), T1(layers 4,10,16), T2 (layers 22,24,26), and U (layers 6,12,18). The layers in the front part of

the modules were interleaved to optimize the photon detection efficiency. The strips in U,V were ganged in pairs in width and the strips in W in groups of 2 to 4 in corners of a module where they were short. In front of the lead stack were 2 plates of .16 cm aluminum separated by .2 cm gaps with the center plane divided into 3.2 cm wide strips at W. These gaps, referred to as massless gaps, served to identify showers that began in the 1.4 radiation lengths of material (primarily the magnet coil) that preceded the lead stack. The lead and aluminum were enclosed in an aluminum shell that contained the liquid argon. Altogether the lead, liquid argon, aluminum, and material preceding the modules were 15.1 radiation lengths thick.

F.2 ELECTRONICS AND CALIBRATION

The strips were run at positive high voltage (usually 3.5 kV except the massless gaps which were at 10 kV) to collect the ionization electrons from the liquid argon. Each channel was isolated from the high voltage supply by a 100 MΩ resistor so that a short in one channel would not affect other channels. The signals were read out via 6.25 nF high voltage blocking capacitors to low noise charge sensitive preamplifiers, pulse shaping amplifiers, sample and hold modules[48], ADCs, and microprocessors (Fig. 35). The six microprocessors[49] did channel by channel conversion of the signal charge collected to the equivalent energy

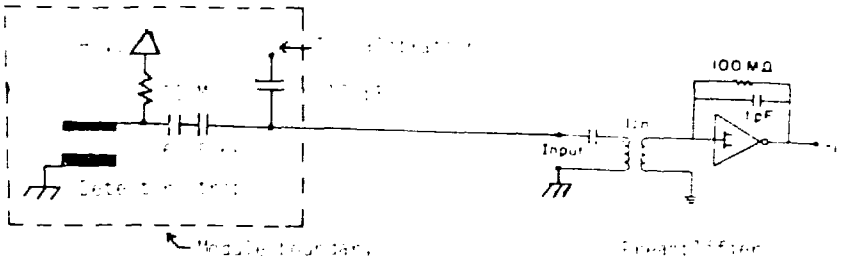

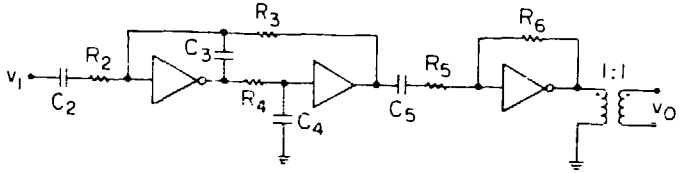

Shaping Amplifier

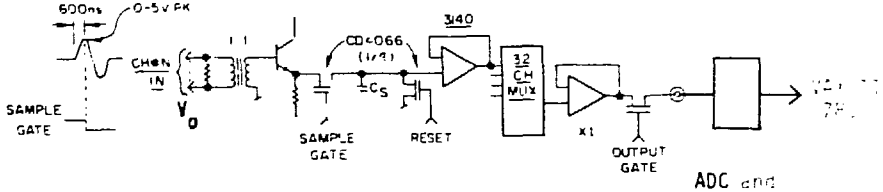

Sample and Hold

ADC and Micro-processor

XBL 803-8588

deposited in the liquid argon. The microprocessors also corrected for the for the gain and offset of each channel as determined by calibration runs and for the ballistic efficiency of the amplifiers. Channels with a signal greater than one rms noise fluctuation were written to magnetic via the online VAX 11/780 computer.

The entire electronics chain for each channel was calibrated by injecting known amounts of charge on 10 pF calibration capacitors located on the low voltage side of the blocking capacitors. The output was read out as for data, and the gain, offset, and rms noise fluctuation were calculated for each channel. It was necessary to correct for leakage of the calibration charge to ground via the blocking capacitor and the detector strip capacitance. These correction factors (precalibration constants) were measured for each channel during construction before enclosure in the aluminum shell. Calibrations were done three times per day, primarily for diagnostic reasons since the electronics were stable over a much longer period of time. The failure rate of the electronics was less than .1% of the 3000 channels per week.

B.3 SHOWER RECONSTRUCTION

The liquid argon shower counters served two distinct purposes in the Mark II detector; they provided for detection and momentum measurement of photons, and they

distinguished electrons from other charged particles. Since these two applications presented different problems for the shower reconstruction routines, they were treated separately.

Charged particles were reconstructed first. A minimum ionizing particle deposited 200-400 MeV of energy uniformly along its track through a liquid argon module. Being a sampling device, a module collected only 12% of the resulting ionization. A hadron acted as a minimum ionizing particle or interacted strongly in the module. An electron showered and nonuniformly deposited its energy with the maximum energy deposition occurring in the front half of a module and with little leakage out the back for SPEAR energies. To obtain maximal liquid argon information for charged particles regardless of how they deposited their energy, tracking information from the drift chambers guided the liquid argon reconstruction. The position where the track passed through each layer of the liquid argon module was projected from the drift chambers. The largest pulse height in that layer within 2-3 strips, depending on depth, of the projected position plus any contiguous group of hits surrounding that strip was associated with that charged particle. The distance of the projected position from the largest pulse height depended on the drift chamber resolution, scattering or interaction of the particle, and shower fluctuations. The maximum distance allowed was determined empirically.

The alternate approach to handling charged particles was to do the liquid argon reconstruction independently of the drift chamber tracking and then match the liquid argon and drift chamber tracks. The reconstruction algorithm described below for photons was only 45% efficient for finding minimum ionizing particles since they deposited only as much energy as a photon of a few hundred MeV. Electrons were detected with an efficiency similiar to photons (see Fig. 5). The loss of information from inefficiency in charged particle reconstruction would have been extremely detrimental to electron-hadron separation.

A goal of photon reconstruction was to maximize the low energy photon detection efficiency. To accomplish this, reconstruction used pulse heights that were close to the level of electronic noise. The rms fluctuations of the noise were measured for each channel in calibration runs, saved, and written on tape for each data run so that they were available to the reconstruction program. Typical rms noise fluctuations were equivalent to approximately .3-.4 MeV of collected energy for the massless gaps, 2.5-3 MeV in F3, and .8-1.2 MeV in the other layers. This is compared to typical signals which ranged from a couple of MeV collected in a channel for a two hundred MeV photon to tens of MeV for photons above one GeV. Since reconstruction worked close to the level of noise, noise fluctuations could create spurious photons. Designing a reconstruction

program was then a process of maximizing the efficiency while minimizing the number of spurious photons. A channel with an up fluctuation of noise could combine with other channels in one of three ways to form a spurious photon: it could combine with channels in other layers with up fluctuations in their noise; it could combine with channels which were correctly reconstructed as part of a real photon or charged particle; or it could combine with energy deposited by a real particle which was missed by the reconstruction program. The number of spurious photons was monitored by using cosmic ray events, which should have had few real photons, collected during normal data taking.

The basic concept of the photon reconstruction was to make a low cut on the pulse height in individual layers to allow for down fluctuations in the energy deposited in any one layer, and then, to limit the number of spurious photons, make a cut on the sum of the energies in several layers. This cut favored the correlated nature of energy deposition by real showers and discriminated against uncorrelated electronic noise.

The program first looked for hits which had a pulse height of at least twice the rms noise. A group was built around a strip by adding channels on each side until one of the following occured: (1) a blank channel was found (one blank channel was allowed if it was a dead channel), (2) a signal of less than twice the rms noise was reached,

(3) the beginning or end of the layer was reached, or (4) there were four channels in the group (six channels were allowed if the energy in the group was large, that is, at least fifteen MeV). In the case of (2), one channel with energy less than twice the rms noise was added to each side of the group if that kept the number of channels in the group under the maximum outlined in (4). The centroid of each group (denoted below by the name of the layer, for example, F1) was calculated as the pulse height weighted average of the position of the strips in the group. The width of the group was calculated as the pulse height weighted rms deviation of the position of the strips from the centroid.

To allow for shower fluctuations, photon candidates were defined by any one of four algorithms: (1) About 80% of the photons were found by requiring a crossing of F1 and/or F2, U, and T1 groups defined by requiring $|F + T1 - 2U| < 1.5$ strip widths (3 strip widths in corners of a module where the U strips were ganged). The sum of the deposited energies in F1 or F2, U, and T1 was required to be at least 7 MeV + 1 MeV times the number of channels in the F1 or F2, U, and T1 layers. (2) To find photons that deposited little energy in F1 or F2 due to shower fluctuations, noise fluctuations, or dead channels, an identical algorithm to (1) was employed except that massless gap groups were used instead of F1 and F2. (3) The third

algorithm designed to find late showering photons required a crossing of F2, U, and T2 groups which again had a total deposited energy of at least 7 MeV + 1 MeV times the number of channels. (4) Finally, early showering photons were found by requiring exactly one T1 group and massless gap group, neither of which had been used by algorithms 1 to 3. Each group was required to have a strip with a deposited energy of at least four times the rms noise. There could not be more than one of each type of group for algorithm (4) because there was no ambiguity resolution without U strips. Though algorithms (2)-(4) accounted for 20% of the total number of photons, they found 40% of the photons below 200 MeV.

After finding a candidate, the program searched the layers not used in the algorithm for deposited energy associated with that shower. The channel with the largest energy deposited within 1.5 strips of the expected position plus any group of hits around it was associated with the candidate. For photons of energy less than six hundred MeV, the F3 layer was not used since the shower was contained before then and the large noise fluctuations characteristic of F3 channels adversely affected the energy scale and resolution.

To reduce spurious photons from noise hits combining with energy deposited by real tracks, two further checks were done. If two showers shared a group in one of the

layers, the energy in that group was apportioned according to the ratio of the unshared energy in the showers. If, after doing this, the total deposited energy in the layers used to find the candidate was not at least ten MeV, the photon candidate was discarded. Any candidate left after this which shared more than one type of layer (for example, both an F and a T) was discarded. Surviving candidates were called photons.

B.4 ENERGY CORRECTIONS

Since the lead-liquid argon modules are sampling devices, it was necessary to convert the energy deposited in the liquid argon to the total energy of the incident particle. In addition, to obtain the optimal energy resolution it was necessary to correct for losses of energy in the 1.4 radiation lengths of material which preceeded the modules (primarily the magnet coil) and for leakage of energy out the backs of the modules. The corrected energy was given by

$$E_{corrected} = \alpha E_{LA} + \Delta E + E_{leak}$$

where E_{LA} is the energy deposited in the liquid argon between the lead planes (the energy deposited in the massless gaps was not included here), α is a module dependent normalization factor, ΔE includes the various corrections discussed below, and E_{leak} is the leakage energy. The

constant α primarily corrected for the fact that ionization in the lead was not collected and, to a lesser extent, for module to module variations in the precalibration constants, lost signal due to electronegative contaminants in the liquid argon, and any overall errors in the calibration. The normalization constant α was determined for each module with high energy electrons from Bhabha events. Typical values were .08, corresponding to a collection of about 12% of the incident particle energy.

The contributions to the correction term were parameterized according to known physical processes (such as ionization losses) or by using the detailed shower Monte Carlo EGS[31] for shower simulation. For electrons the correction was

$$\Delta E = \Delta E_I + \Delta E_{RAD} + \Delta E_{MG}$$

ΔE_I corrected for ionization loss by the primary electron in the coil (coil henceforth refers to all material which preceeded the lead stack) and was given by[50] $\Delta E_I = 62.4/\cos\theta_c$ where θ_c was the angle of incidence with the coil. ΔE_{RAD} was the average radiative loss in the coil, that is, energy lost because the electron began to shower in the coil. Its form was determined by Monte Carlo to be $\Delta E_{RAD} = (52+72.5\log(E/600))/(\cos\theta_c)^{2.4}$ where $E = \alpha F_{LA}$. The good signal to noise ratio of the massless gaps permitted their use to correct the average radiative loss by

counting the number of minimum ionizing particles that left the coil and passed through the massless gaps. The term ΔE_{MG} did this correction and was given by $\Delta E_{MG} = (n-\bar{n})s$ where n and $\bar{n}$ are the observed number and calculated average number of minimum ionizing particles in the massless gaps and s is the Monte Carlo determined correlation between the pulse height in the massless gap and the radiative loss in the coil. These parameters were given by

$$n = \frac{\text{massless gap pulse height}}{3.38} \cos \theta_{MG}$$

$$\bar{n} = 3.5 + 4.4 \ln(E/600)$$

$$s = 8.5 + 10.6 \ln(E/600)/\cos^{2.4} \theta_c$$

where θ_{MG} is the angle of incidence of the electron with the massless gaps which could differ from θ_c since the massless gaps were planar whereas the coil was cylindrical. Note that n was not necessarily an integer.

For a photon, the correction depended on whether it converted in the coil or not. A photon was considered to have converted if the pulse height in the massless gaps was at least four times the rms noise fluctuations. If a photon actually did not convert, there would be no loss of energy in the coil. However, a 5 MeV correction was made for the very small fraction of the converted photons which because of shower or noise fluctuations deposited little energy in the massless gaps and hence were classified as

nonconverted photons. For converted photons, the correction was

$$\Delta E = \Delta E_{RAD} + \Delta E_{MG}$$

This is the same as for electrons except the ionization term is absent and the other terms are parameterized differently, given as

$$E_{RAD} = (86 + 44 \ln(E/600))/\cos^{1.4}\theta_c$$

$$E_{MG} = (n-\bar{n})s$$

$$n = \frac{\text{massless gap pulse height}}{3.38} \cos\theta_{MG}$$

$$\bar{n} = 3.53 + 3.03 \ln(E/600)$$

$$s = 15.5 + 18.3 \ln(E/600)$$

The leakage term was

$$E_{leak} = E(a + b \ln(E/600))\ e^{-c/\cos\theta_{MG}}$$

were a, b, and c were constants that depended on whether the particle was an electron, unconverted photon, or converted photon. Furthermore, since for photons with energy less than 600 MeV, the energy deposited in the F3 layer was excluded, the three constants were different for these photons. Table 6 summarizes the various cases. For low energy particles, E_{leak} could become negative in which case no correction was made.

Finally, two small empirical corrections determined by studying systematic differences between fit and measured energies in $\psi \to \pi^+\pi^-\pi^0$, $\psi \to 2\pi^+2\pi^-\pi^0$, and $\psi' \to \psi\eta \to \ell^+\ell^-\gamma\gamma$ events were made. For photons at large z ($|z| > 1.488$ m) the energy was multiplied by $1+.179(|z|-1.488m)$. To correct for the fact that low energy photons were more likely to be detected if there was an up fluctuation in the deposited energy due to shower statistics, a correction of $\Delta E_{emp} = 25-.042E$ was added to photons of energy less than 600 MeV.

Figs. 36-40 show the corrected energies of various electrons and photons over a wide range of energies with all distribution peaking at the correct values. These distributions are discussed in more detail in the next section in connection with the energy resolution.

Type of Particle	a	b	c
Electrons	3.42	1.69	4.56
Converted photons			
E < 600	1.56	1.47	3.38
E > 600	1.56	1.47	4.28
Unconverted photons			
E < 600	3.11	3.60	3.38
E > 600	3.11	3.60	4.28

Table 6. Parameters used in calculating energy leakage correction.

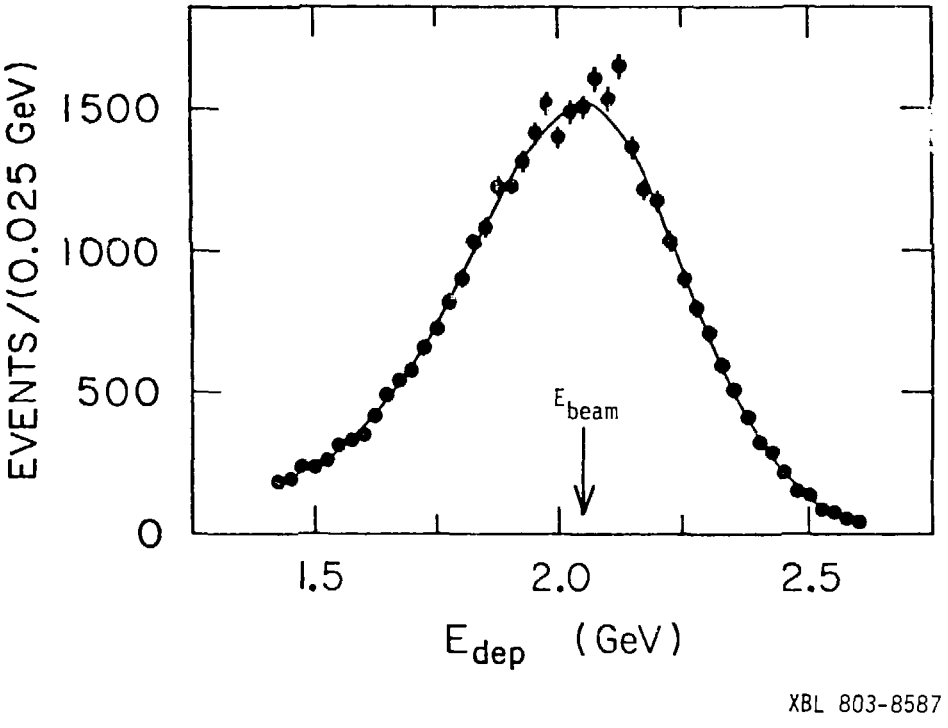

Fig. 36. Energy deposited in the liquid argon system by electrons from Bhabha scattergin events. The curve corresponds to an energy resolution of $11.5\%/\sqrt{E}$. The distribution is non-gaussian because of radiative effects.

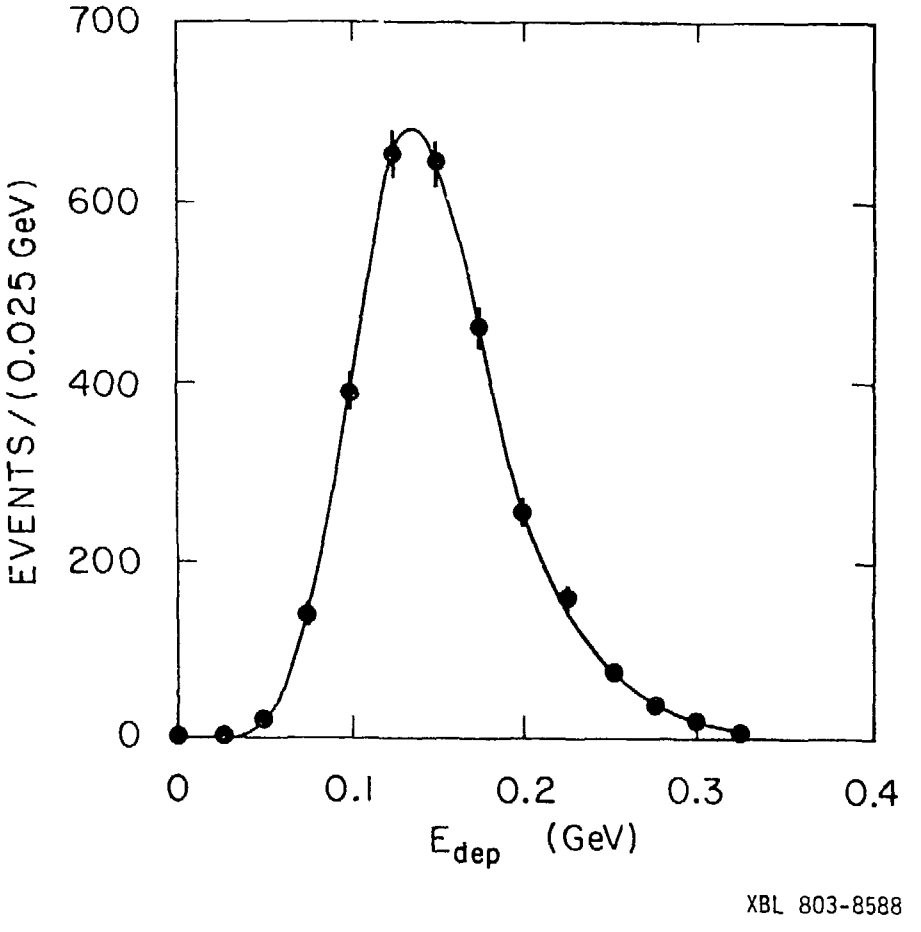

Fig. 37. Energy deposited in liquid argon system by low energy electrons from gamma conversions. Curve corresponds to an energy resolution of $11\%/\sqrt{E}$.

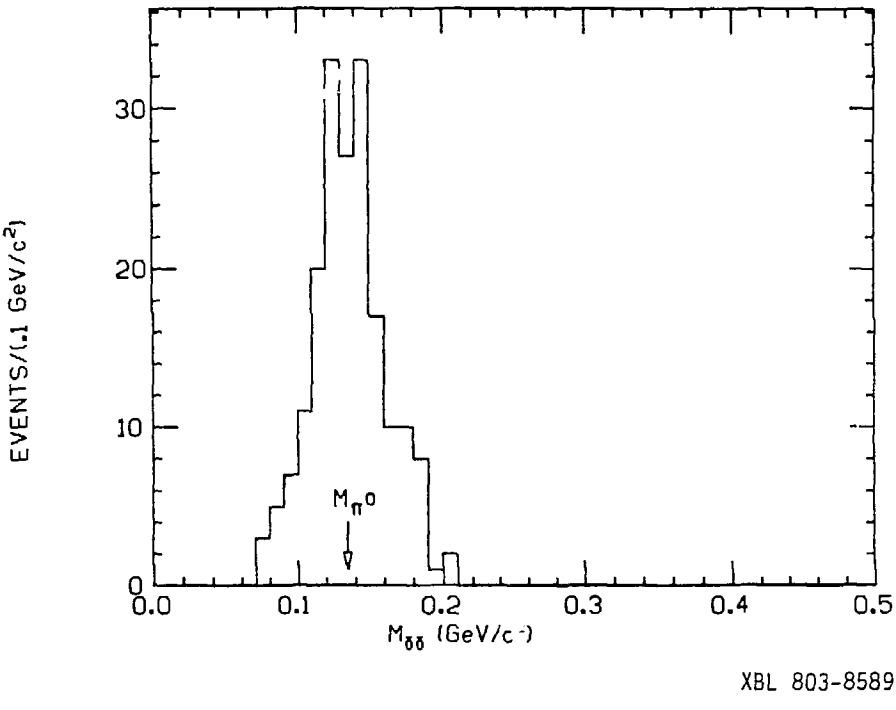

Fig. 38. Gamma-gamma invariant mass of photons identified from a kinematic fit to $\psi \to \pi^+\pi^-\pi^0$ or $\psi \to 2\pi^+2\pi^-\pi^0$ events.

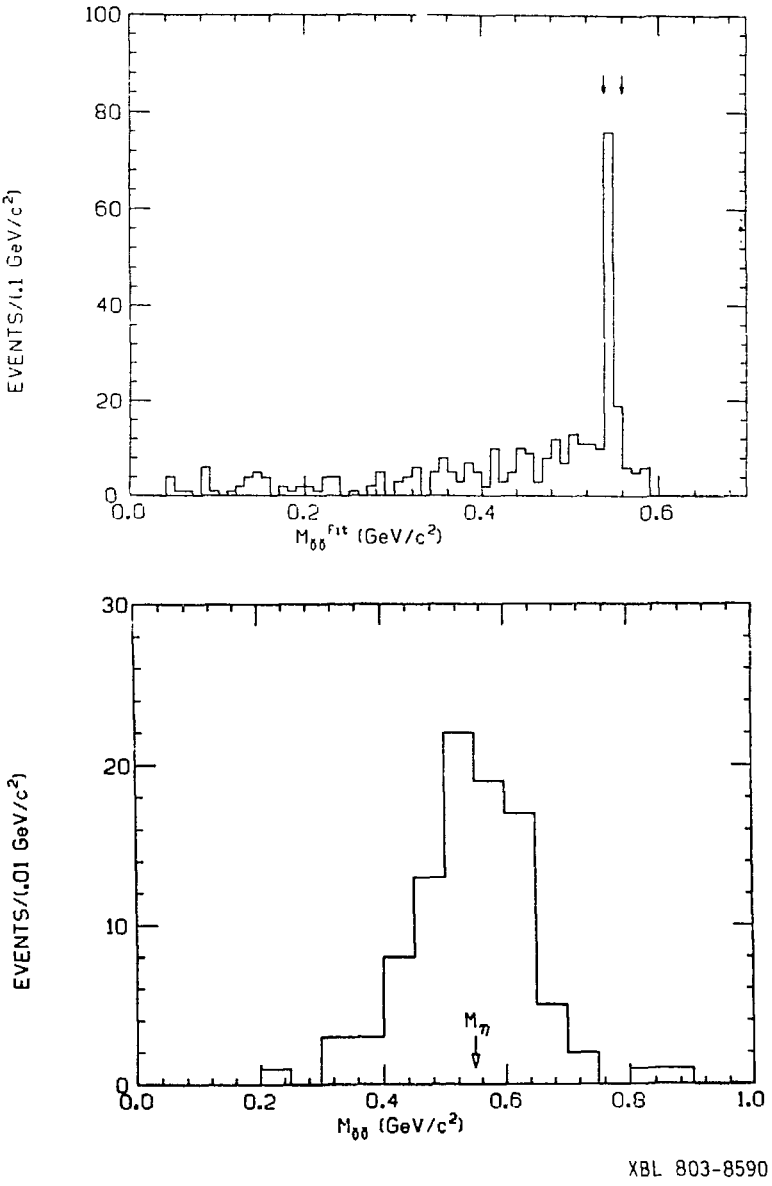

Fig. 39. (a) Gamma-gamma invariant mass for events fit to $\psi' \rightarrow \gamma\chi_{c1}, \chi_{c1} \rightarrow \ell^+\ell^-\gamma$ where ℓ is a lepton. A very clear η signal is seen. (b) Gamma-gamma invariant mass for events identified from (a) as $\psi' \rightarrow \gamma\eta$.

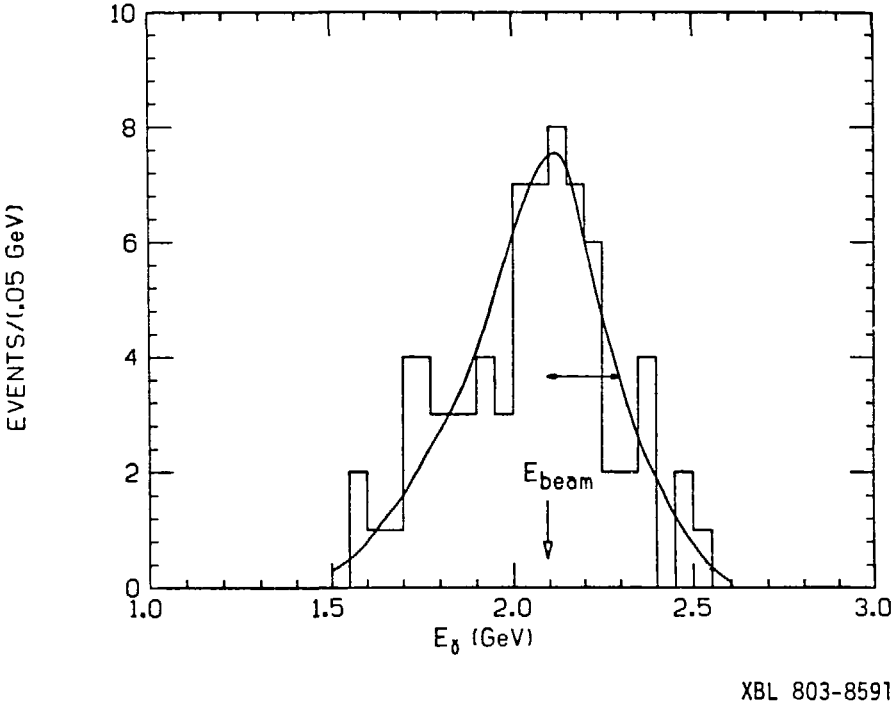

Fig. 40. Photon energy spectrum for $e^+e^- \to \gamma\gamma \to \gamma e^+e^-$.

B.5 PERFORMANCE

The energy resolution of the liquid argon system was 11-13%/$\sqrt{E}$ depending on the type and energy of the particle. The was as good or slightly better than expected from calculations and from measurements with a full-size prototype module with a similar amount of preradiator in a test beam. Electron energies were measured using bhahba events (Fig. 36) and photon conversions (Fig. 37). The resolution for electrons was 11.5%/$\sqrt{E}$ over their entire energy range. Comparison of measured energies with values from kinematic fits of events of the type $\psi \rightarrow \pi^+\pi^-\pi^0$, $\psi \rightarrow 2\pi^+2\pi^-\pi^0$, and $\psi' \rightarrow \psi\eta \rightarrow \ell^+\ell^-\gamma\gamma$ (Figs. 38 and 39) measured the low energy photon resolution to be 12%/$\sqrt{E}$ for photons which did not convert in the coil and 13%/$\sqrt{E}$ for those which did. The resoltuion was greater for converted photons due to uncertainties in the corrections for losses in the coil. Photons from $e^+e^- \rightarrow \gamma\gamma \rightarrow \gamma e^+e^-$ events gave a high energy photon resolution (Fig. 40) of 12%/$\sqrt{E}$.

The angular resolution ranged from 3.6 mrad (20% of a strip width) for high energy electrons to about 8 mrad for low energy photons. The angular resolution was better for higher energy particles because their showers spread over several strips per layer allowing a more accurate determination of the centroid. For particles of energy less than 1 GeV, usually only one or two channels in a layer had a signal.

The efficiency was measured from $\psi \to \pi^+\pi^-\pi^0$ and $\psi \to 2\pi^+2\pi^-\pi^0$ events where at least one of the photons from the pi zero was detected. A two constraint fit was done on the charged particles' momenta and one of the photon's momentum to determine the direction and energy of the other photon. The efficiency was the fraction of the events where a photon with the expected energy and position was found. Fig. 5 shows the measured efficiency after removing geometrical effects. The curve is the result of a detailed Monte Carlo calculation which used the shower code EGS[31] to deposit energy according to the module geometry and then analyzed this data with the same reconstruction program as was used for real data. The efficiency decreases at low energies for primarily three reasons. First, there was the presence of the 1.4 radiation length thick magnet coil. Low energy photons that began showering in the coil deposited little energy in the lead stack to be used for reconstruction. Second, different layers measured the energy deposited at different depths. Reconstruction was then affected by shower fluctuations that caused little energy to be deposited at a given depth. Finally, noise fluctuations could reduce small signals to below the minimums required.

The number of spurious photons from noise combining with real deposited energy was reduced by eliminating photons that were within 36 centimeters (measured at the module) of a charged track. Even when this was done, the

algorithms above found at least one photon in 5-10% of the cosmic ray events. This rate was checked by using Bhabha and mu pair events, and the agreement was good. Bhabha events have real photons from radiative processes, but most of these photons were eliminated by the 36-centimeter cut and the rate was corrected for the those remaining. Since spurious photons could be formed from energy deposited by real tracks, the probability of creating a spurious photon depended on the number of particles in the event. This was measured by looking for extra photons in events $\psi \rightarrow \pi^+\pi^-\pi^0$. A spurious photon was found in 13 + 2% of these events. Fig. 41 shows the photon spectrum for hadronic events compared to that for cosmic ray events.

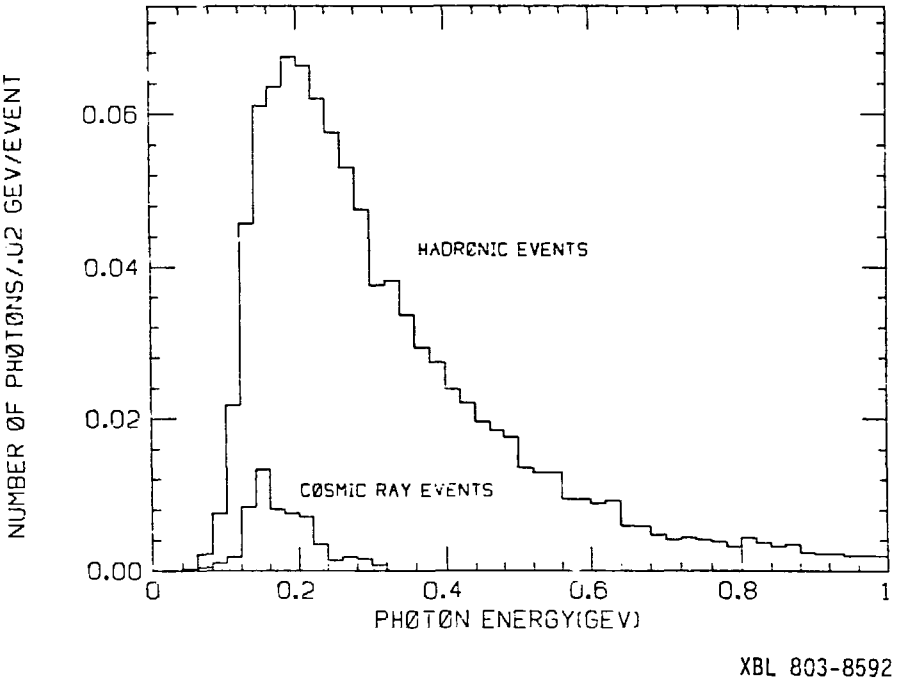

Fig. 41. Typical photon spectrum from hadronic events and from cosmic ray events normalized to the same total number of events.

B.6 ELECTRON-PION SEPARATION

Electron-pion separation in the Mark II detector was done using a method known as "Recursive Partitioning for Nonparametric Classification."[55] This is a powerful classification method when the distributions of the measured quantities are unknown, as for the complicated phenomena of showering electrons and strongly interacting pions, so that maximum likelihood methods cannot be used. It uses a set of known members (training vectors) of the classes to be separated to arrive at a decision rule which minimizes the probability of incorrectly identifying the class.

The decision rule is a binary tree as illustrated in Fig. 42. A particle to be classified is started at the top of the tree. It proceeds left (right) at a branch point if a measured property of the particle is greater than (less than or equal) a predetermined value. A particle is classified as an electron, pion, or ambiguous depending on which final branch of the tree is reaches. Once the structure of a tree has been determined, classification is computationally very fast.

To construct a tree, each observation is assigned a position in a multidimensional space spanned by the quantities measured (x_i). Consider, for a moment, a one dimensional example in which $f_1(x)$ and $f_2(x)$ are the distribution functions of the two classes and $F_1(x)$ and $F_2(x)$ are the cumulative distributions, that is,

$$F(x) = \int_0^x f(y)\, dy.$$

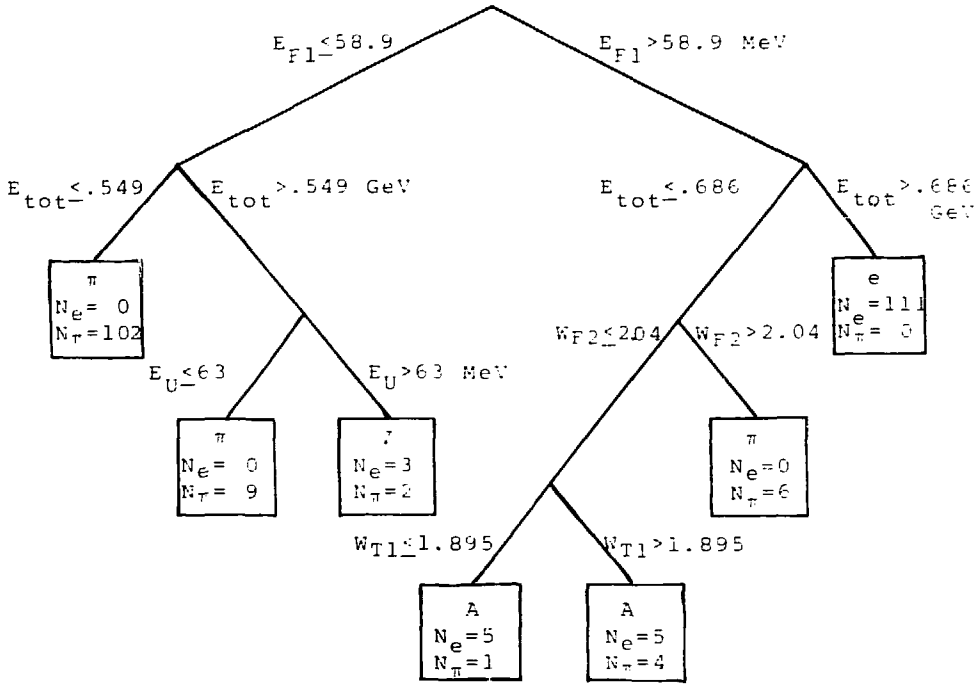

Fig. 42. Simple example of a binary decision tree for separating electrons and pions of momentum from .9 to 1.2 GeV/c. Each terminal node is labeled with the classification of particles that reach there (electron(e), pion(π), or ambiguous(A)) and the number of electron and pion training vectors in that terminal node. Actual electron-pion separation trees were much more complicated.

The best way to partition the x axis with a single cut that minimizes misidentification is to cut at the value of x (denoted by x*) that maximizes $|F_1(x) - F_2(x)|$. The quantity $|F_1(x^*) - F_2(x^*)|$ is known as the Komolgorov-Smirnoff distance. Each subinterval can then be partitioned again (hence recursive partitioning) by cutting at the point that corresponds to the Komolgorov-Smirnoff distance in that subinterval. When the distribution functions are not known (hence nonparametric classification), the cumulative distributions are estimated from the training vectors by

$$F_i(x) = \begin{cases} 0 & x < x_1^i \\ k/n & x_k^i < x < x_{k+1}^i \\ 1 & x < x_n^i \end{cases}$$

where x_k^i is the kth training vector of class i arranged in ascending order and n is the number of training vectors in the class.

Partitioning in several dimensions is done by cutting on the variable x_j that has the maximum Komolgorov-Smirnoff distance. Each subspace thus formed is then partitioned by cutting on the variable that has the maximum Komolgorov-Smirnoff distance in that subspace. Each partitioning of a subspace corresponds to a branch point of the decision tree. The program that constructs the trees automatically considers linear combinations of the variables as possible directions of separation. Partitioning is continued in the subspaces formed until one of the following is encountered. (1) A subspace has training vectors of only one class.

This is a region of the space in which the two classes do not overlap and no further division is necessary. (2) Further division results in Komolgorav-Smirnoff distances which do not represent significant differences in the cumulative distributions. (3) Further division would result in subspaces containing less than a nininun number (determined by the user for the application) of training vectors. If the number of is too small, the estimation of the distributions becomes sensitive to statistical fluctuations of the training vectors. Subspaces that are not divided further are called terminal buckets and correspond to the final ends of branches of the decision tree.

The class identification assigned to each terminal bucket depends on the relative populations of the training vectors in that bucket as given by

$$R_1 = N_1/(N_1 + N_2)$$

$$R_2 = 1 - R_1$$

where N_1 and N_2 are the number of training vectors of each class in the terminal bucket. A threshold value R* is set for the entire tree and each terminal bucket is classified as follows:

if	$R_1 > R^*$	Class=1
	$R_2 > R^*$	Class=2
	otherwise	Ambiguous.

The ambiguous buckets are regions occupied by both classes where one is willing to suffer an inefficiency in order to

reduce misidentifications. The threshold is determined by scanning the results of the decision tree and maximizing the efficiency while minimizing the misidentification.

In one method of measuring the efficiencies and misidentification probabilities, known as cross-validation, a fraction of the training vectors (for example, 10%) are split off and the remaining ones are used to build a tree. The training vectors split off are classified by the tree giving the probabilities that class 1(2) is called class 1(2) or class 2(1). This is repeated by splitting off different fractions to measure all nuances in the data. The final tree is then constructed using the full set of training vectors.

For electron-pion separation the variables were primarily the information measured by the liquid argon system. The coordinates used were the energy deposited in each of the seven layers, the transverse width of the shower in each layer, the track momentum measured from the drift chambers, the angle of the particle momentum relative to liquid argon module, the chi square of the match between the position of the liquid argon shower and the position projected from the drift chambers, the TOF weight to be an electron versus a pion for particles with momentum less than .5 GeV/c, the pulse height weighed average shower depth in the liquid argon module, the longitudinal spread of the shower, the total energy deposited in the module

divided by the momentum, the energy in the front of the module $((2E_{MG} + E_{F1} + E_{F2} + E_{T1} + E_U)/p)$, and an empirically found variable defined as $E_{F1}(E_{T1} + E_U)/p$. Some of the above coordinates were found to have little separating power, but it does not hurt to give such superfluous coordinates to the tree building program as they are simply ignored.

The middle and high momentum (> .7 GeV/c) electron training vectors came from radiative Bhabhas identified as being opposite a particle that had a momentum close to the beam energy ($.85 < p/E_{beam} < 1.08$) and having a large energy deposited in the liquid argon system ($.58 < E_{LA}/E_{beam} < 1.2$). The low momentum electrons came from gamma conversions the beam pipe.

The pions came from two and four charged particle decays of the psi which had a missing mass of less than .63 GeV/c corresponding to $\psi \to \pi^+\pi^-\pi^0$ and $\psi \to 2\pi^+2\pi^-\pi^0$. Events with two tracks with a cosine of their opening angle greater than .99 were not used in order to eliminate contamination from gamma conversions. To reduce contamination from $e^+e^- \to e^+e^-\gamma$, events with two tracks and a photon of energy greater than .5 GeV or identified as $e^+e^-\gamma$ by a scan of events were discarded. In the four track case, events in which the linear sum of the four particles was greater than 3 GeV were eliminated to guard against $e^+e^- \to e^+e^-e^+e^-$. Finally, the TOF system was used to remove kaons and protons.

Decision trees were constructed for the momentum bins .3-.4, .4-.5, .5-.7, .7-.9, .9-1.3 and 1.3-1.5 GeV/c. It was important to have a large number of training vectors in each bin to minimize problems of statistical fluctuations in the terminal buckets, to accurately identify the distributions where the electrons and pions overlapped closely, and to estimate the distributions in regions that were sparsely populated. Each of the momentum bins had 1000-1500 training vectors of each type from data taken during the spring of 1978. Figs. 9 and 10 show the results for classifying data taken during the fall of 1978. The statistical errors are 1-2%. Results for classifying electrons and pions from data taken during the spring of 1978 and the spring of 1979 agree with results of Figs. 9 and 10 within 2-3%.

Several possible biases have to be considered. If the samples of training vectors were not pure, the trees lead to incorrect misidentification probabilities. From careful analysis and scanning of events, the Bhabha electron sample was thought to have very few hadrons in it. For gamma conversions, the primary identifying feature was the small opening angle of the two tracks so that random coincidences of two pions could simulate this. The pion contamination in the gamma conversion electrons was estimated by comparing results from gamma converson electrons with results from Bhabha electrons in a region around .7 GeV/c where

they overlapped. The pion contamination of the gamma conversion electrons was estimated to be about 2%. It was difficult to eliminate electrons from $e^+e^- \rightarrow e^+e^-\gamma$ from the pion sample without losing high momentum pions. However, the rate for this process is small and the cuts reduced the contamination to an estimated 2-3%. A second possible bias was that the angular distribution of the Bhabha electrons was much more peaked at small polar angles than that of particles from hadronic events. To minimize this effect, samples of electrons were selected that had the same angular distribution as hadrons. Another possible bias was the fact that within a momentum bin the momentum spectra of the electrons and pions were not the same so that cuts on the momentum could cause an inaccuracy. An examination of the trees showed that this was not a problem.

Since there were no pion training vectors above 1.5 GeV/c, the tree built from 1.3-1.5 GeV/c was used for particles above that. This was not a problem for electrons since samples of them existed at all attainable momentum and they could be measured. It was possible, however, that this was not a good procedure for the pions. To correct for this for the $\tau \rightarrow \pi\nu$ analysis, a special tree was built from 1.3-1.5 GeV/c using only coordinates that should scale with momentum, namely, the energy deposited in the massless gap, Fl, Tl, and U layers and the total energy deposited (E_{tot}) divided by the momentum. For higher momenta the

cuts in the tree were scaled by the momentum divided by 1.4 GeV/c (E_{tot}/p was not scaled, of course). The validity of this procedure was checked in two ways. First, a similiar tree was built fror 1-1.1 GeV/c and it was checked that the efficiencies and misidentification probabilities for pions up to 1.5 GeV/c and for electrons up to 2.5 GeV/c were flat. Secondly, it was checked that for the 1.3-1.5 tree, electrons scaled from 1.5 to 2.5 GeV/c and pions scaled backwards down to 1 GeV/c. All efficiencies and misidentification probabilities were found to be very flat except to a slight improvement in the electron misidentification probability at higher momentum.

REFERENCES

1. In all particle reactions, the charge conjugate reaction is also implied. Electron, muon, and tau neutrinos and antineutrinos are all denoted by ν and the appropriate ones are inferred from conservation of electron, muon, and tau number. For example, $\tau \to e\nu\nu$ implies $\tau^- \to e^-\bar{\nu}_e\nu_\tau$ and $\tau^+ \to e^+\nu_e\bar{\nu}_\tau$.

2. The luminosity is the factor that multiplies the cross section to obtain the event production rate.

3. M. L. Perl et al., PRL 35, 1489 (1975); M. L. Perl et al., Phys. Lett. 63B, 466 (1976)

4. M. Cavalli-Sforza et al., PRL 36, 558 (1976)

5. G. J. Feldman et al., PRL 38, 117 (1977)

6. J. Burmester et al., Phys. Lett. 68B, 297 (1977)

7. J. Burmester et al., Phys. Lett. 68B, 301 (1977)

8. R. Prandelik et al., Phys. Lett. 73B,109 (1978)

9. W. Bacino et al., PRL 41, 13 (1978)

10. W. Bartel et al., Phys. Lett. 77B, 331 (1978)

11. Y. S. Tsai, SLAC-PUB-2105, (1978)

12. W. Bacino et al., PRL 42, 749 (1979)

13. A. M. Cnops et al., PRL 40, 144 (1978)

14. S. P. Rosen, PRL 40, 1057 (1978)

15. Due to a free parameter in the calculation of $\tau \to e\gamma$, the possibility that ν_τ is ν_e is not strictly eliminated.

16. H. Fritzsch, Phys. Lett. 67B, 451 (1977); D. Horn and G. G. Ross, Phys. Lett. 67B, 460 (1977); G. Altarelli et al., Phys. Lett. 67B, 463 (1977)

17. S. A. Adler, Phys. Rev. 177, 2426 (1969); J. S. Bell and R. Jackiw, Nuovo Cimento 60A,47 (1969)

18. H. B. Thacker and J. J. Sakurai, Phys. Lett. 36B, 103 (1971)

19. Y. S. Tsai, Phys. Rev. D4, 2821 (1971)

20. F. J. Gilman and D. H. Miller, Phys. Rev. D17, 1846 (1978)

21. N. Cabibbo, PRL 10, 531 (1963)

22. These values were calculated by using the partial widths from Table II of Tsai[19] for $e\nu\nu$, $\mu\nu\nu$, $\pi\nu$ (with a misprint corrected), and $K\nu$ and using Gilman and Miller's[20] values of $B_{\rho\nu}/B_{e\nu\nu}$ and $B_{4\pi\nu}/B_{e\nu\nu}$. The K* was calculated from Tsai's formula using Gilman and Miller's number for $B_{\rho\nu}$. Finally, $B_{\geq 5\pi\nu}$ was taken to be Tsai's value for the $\tau \rightarrow \nu$+hadron continuum (corrected for the fact that he neglected three colors for the e+e- data) minus the $4\pi\nu$ contribution.

23. These values are from a fit to the world's data on B_e, B_μ, $B_{1\ \text{hadron}}$, and $B_{\geq 3\ \text{hadrons}}$ done by G. J. Feldman in SLAC-PUB-2230.

24. S. Yamada, "Recent Resulst from DASP" in Proceeding of the 1977 International Symposium on Lepton and Photon Interactions at High Energies, Hamburg, August 25-31, 1977, edited by F. Gutbrod, (DESY, Hamburg, 1977)

25. G. J. Feldman, talk given at the International Conference on Neutrino Physics - Neutrinos '78, Purdue University, April 28-May 2, 1978, and SLAC-PUB-2138 (1978)

26. G. Alexander et al., Phys. Lett. 78B, 162 (1978)

27. W. Bacino et al., PRL 42, 6 (1979)

28. D. Hitlin, talk given at the XIX International Conference on High Energy Physics, August 23-30, 1978, Tokyo, Japan.

29. G. S. Abrams et al., PRL 43, 1555 (1979)

30. W. Davies-White et al., Nuclear Instr. and Methods 160, 227 (1979)

31. R. L. Ford and W. R. Nelson, EGS Code, SLAC Report No. 210 (1978)

32. H. Brafman et al., IEEE Transactions on Nuclear Science NS 25, 692 (1978)

33. T. M. Himel, PhD. Thesis, SLAC Report No. 223 (1979)

34. J. L. Siegrist, PhD. Thesis, SLAC Report No. 225 (1979)

35. J. H. Friedman, IEEE Transactions on Computers, April 1977, 404

36. J. D. Jackson and D. L. Scharre, Nucl. Instr. and Meth. 128, 13 (1975)

37. F. A. Berends et. al., Nucl. Phys. B68, 541 (1974); S. M. Swanson, Phys. Rev. 154, 1601 (1967)

38. F. A. Berends et. al., Nucl. Phys. B57, 381 (1973)

39. S. J. Brodsky et. al., Phys. Rev. D4, 1532 (1971); J. E. Zipse, Ph.D. Thesis, LBL Report No. 4281

40. For four charged particles with a total charge of zero, there are four ways of putting two of them together so that they have opposite charges and two ways such that they have the same charge.

41. $B_\mu = .973\ B_e$ was assumed in this fit

42. R. Brandelik et al., Zeitschrift fur Physik C1, 233 (1974)

43. J. A. Jaros et al., PRL 40, 1120 (1978)

44. G. S. Abrams et al., PRL 44, 10 (1979)

45. R. H. Schindler, PhD. Thesis, SLAC Report No. 219 (1979)

46. The first error is statistical and the second is systematic.

47. W. J. Willis and V. Radeka, Nucl. Instr. and Meth. 120, 221 (1974)

48. E. L. Cisneros et al., IEEE Transactions on Nuclear Science NS 24, 413 (1977)

49. M. Briedenbach et al., IEEE Transactions on Nuclear Science NS 25, 706 (1978)

50. All energies in this section are given in MeV.